3. Metal Diffusion inside Semiconductor Bulk

3.1 Introduction

This *Chapter* will be devoted to the analysis of the metal diffusion influence on semiconductor gas sensor materials. Metal diffusion inside semiconductor bulk is one of the possible ways of metal distribution that we will study in this *Thesis* work. As it has been already reported in several works, there are some metal species that can occupy interstitial positions or induce structural changes in metal oxide structures, as in the case of Nb, V and Ce loaded to TiO_2 [1, 2, 3]. In this *Chapter* the Nb/TiO_2 systems have been studied, since there are strong evidences that Nb atoms enter substitutionally inside TiO_2 structure occupying Ti vacants. The effect of Nb doping in titania lattice and its importance for oxygen sensors have been recently pointed out by a high number of works [4, 5, 6, 7, 8] indicating higher device sensitivity [9] at lower working temperatures [10, 11].

Likewise recent studies have shown the feasibility of using Nb/TiO_2 as surface conductance CO sensors [12]. And moreover, G. Sberveglieri et al. found that Nb/TiO_2 thin films could be used to monitor methanol selectivity at ppm levels with negligible sensitivity to interfering gases such as benzene, CO and NO_2 [13]. For both applications, nanosized grains of sensing material are preferred to increase the specific surface exposed to gas.

Although many works insist on the influence of Nb on strain, grain size evolution and anatase-to-rutile transformation and their consequences on sensing devices [6, 8, 9, 10, 12, 14, 15], no systematic research work on this field is found up to our knowledge. Therefore, this work provides useful data for technological improvement of sensor devices as well as for the scientific understanding of anatase to rutile transformation and the role of Nb in all these mechanisms.

We have divided this *Chapter* in two main parts. After introducing the experimental details, we will continue by offering a complete study of the Nb influence in TiO_2 phase transition from anatase metastable phase to rutile stable phase (*Section 3.3*). This analysis will be carried out using spectroscopic techniques such as Raman and XRD. In this way, we will analyze the influence of annealing temperature as well as the influence of the metal loading percentage in the anatase to rutile phase transition. At the end of this *Section*, we will perform an accurate comparison of the spectroscopic results with those obtained by Selected Area Electron Diffraction, trying to determine the possible segregation of Nb at high loading values.

The last part of the *Chapter* (*Section 3.4*), will be devoted to an extensive study of the Nb/TiO_2 samples nanostructure by using TEM and HRTEM. In a first approach, we will analyze the TiO_2 grain size evolution with Nb loading percentage at low (600 °C) and high (900 °C) annealing temperatures. And finally, HRTEM will help us to determine the phase transition and growth mechanisms of the TiO_2 nanoparticles.

The results obtained in the previous *Sections* will be discussed in *Section 3.5* and summarized in the final conclusions (*Section 3.6*).

In the following, we will show a brief description of the sample preparation method used in order to obtain the Nb/TiO_2 samples (Laser Induced Pyrolisis), summarizing in a table the main characteristics of the samples used in this *Chapter* work. Moreover we will numerate the analytical techniques utilized for our analyses and we will explain the main reasons for the use of every one of them.

3.2 Experimental Details

The first studies in our laboratory in the context of SGS materials characterization were done in the frame of the EU project NANOGAS. In this project, the grain size distribution and agglomeration state of the Nb/TiO$_2$ nanopowders were measured in order to compare the results with the active surface measurements carried out by means of BET (Brunauer-Emmet-Teller). These powder samples of niobium-titanium oxides were obtained by laser-induced pyrolisis, although recent works found in literature have shown that Nb/TiO$_2$ samples grown by both, laser-induced pyrolisis [8] and sol-gel methods [11, 13], to obtain these SGS systems, offer similar results with no appreciable differences after sample characterization. The process of laser-pyrolisis is based on the pyrolisis of suitable precursors induced by the absorption of a cw-CO$_2$ laser radiation. The detailed description of the operation principles and the experimental apparatus were already reported [16]. Briefly, a CO$_2$ laser beam perpendicularly intersects a reactant stream, defining a well-localized reaction zone that allows the growth of nanometric powders with a narrow size distribution. Vapors of Ti-isopropoxide were used for the synthesis of pure TiO$_2$, while controlled amounts of Nb-isopropoxide vapors were added to the reactant stream for the production of Nb-Ti oxides.

To start our work, we have utilized a set of low growth temperature seed Nb/TiO$_2$ samples synthesized in the frame of the previous European project, NANOGAS.[♣] We have extended the analysis accounting for the sample evolution with the annealing temperature. In this way, we have submitted the seed set of samples to a temperature treatment in the range 600º C-900º C. The set of samples grown in order to perform our analysis is

---

[♣] The seed Nb/TiO$_2$ samples were provided by CISE (Milano, Italy).

that shown in *table 3.1*. Notice that samples selected have different contents of Nb. All samples have been annealed in different stages from 600 °C to 900 °C in steps of 50 °C, obtaining an independent set of temperature graded samples for every additive concentration value used. The samples were submitted to a 10 °C/min temperature ramp until we reached the selected temperature. Once we obtained the desired temperature, the samples were annealed during 2 hours in air. After annealing, a free cooling was applied to samples. In the following, samples will be named with the letter of the corresponding set plus the number of the thermal treatment temperature; i.e.: C850 (denotes a sample from set C annealed at 850 °C). For the annealing, a muffle furnace Carbolite 1100 with Eurotherm PID temperature controller was used.

The analysis of the Nb influence in TiO_2 anatase to rutile phase transition has been studied by using Raman and XRD. Both techniques are of great utility in order to quantify the anatase/rutile percentage in every one of the samples annealing stages. In this way, we have analyzed the whole samples (from 600 to 900 °C every 50 °C) in every set (A-C). SAED results for all sets of samples (A-C) at low (600 °C) and high (900 °C) temperatures, have been compared with those obtained by using the spectroscopic techniques. TEM and HRTEM have been also applied in order to carry out the last part of the *Chapter* (*Section 3.4*). The use of nanoscopic techniques has allowed us to study the nanostructural properties of the anatase-rutile phase transition.

Samples	**Nb/Ti at. %**	**$T_{annealing}$ (ºC)**
A	0.0	600-900 ºC
B	2.9	600-900 ºC
C	3.4	600-900 ºC
D	10.9	600-900 ºC
E	24.5	600-900 ºC

Table 3.1 Description of sample metal loading concentrations and annealing temperatures applied in every set.

3.3 Anatase to Rutile Phase Transition in Nb/TiO_2

This part of the *Chapter* has been devoted to the study of the TiO_2 transition from the anatase metastable phase to the rutile stable phase. Firstly we have analyzed by spectroscopic techniques such as XRD and Raman the influence of the annealing temperature (*Section 3.3.1*) in order to obtain a qualitative overview of the phase transition evolution. In a second part (*Section 3.3.2*) we have compared the results obtained for different Nb loading percentages at fixed annealing temperatures. In *Section 3.3.3*, we have presented the quantitative results about Anatase/Rutile ratio evolution. And finally, in *Section 3.3.4*, we have compared all the former results with those obtained by SAED.

3.3.1 Influence of the Annealing Temperature

To carry out the analysis made in this *section* we have selected three characteristic samples. The first sample analyzed is sample A, where no additive has been loaded. The next sample is one of the low Nb loaded samples (Sample B). Finally, the last sample corresponds to one of the high Nb loaded samples (Sample E). In a first approach we have obtained the Raman spectra of all of them, which is compared with XRD results. In *table 3.2*, we present the most important Raman peaks in synthetic titania polymorphs [17]. A complete summary of the most common XRD peaks is also given in *table 3.3*.

All the spectra shown in the *figures* of the following *sections* have been obtained at different temperatures (from 600 °C to 900 °C in 50 °C steps). Intensities are shown in arbitrary units and peaks height is not normalized, since at this point we just want to show the qualitative evolution of TiO_2 phases (a quantitative analysis is made in *Section 3.3.3*).

Rutile (cm^{-1})	Anatase (cm^{-1})
143 (w) B_{1g}	144 (vs) E_g
235 (m)	198 (w) E_g
273 (sh)	320 (vw)
320 (w)	397 (m) B_{1g}
357 (w)	516 (m) B_{1g}
449 (s) E_g	639 (m) E_g
610 (s) A_{1g}	695 (vw)
832 (w) B_{2g}	795 (w) B_{1g}

Table 3.2 Raman spectra of synthetic titania polymorphs (cm^{-1}). Letter notations means: vw-very weak peak, w-weak, m-medium, s-strong, vs-very strong and sh-shoulder [17].

Rutile 2q	(hkl)	Anatase 2q	(hkl)
27.44	110	25.30	101
36.08	101	36.95	103
39.19	200	37.79	004
41.24	111	38.57	112
44.04	210	48.04	200
54.32	211	53.88	105
56.62	220	55.06	211

Table 3.3 XRD spectra of the most common peaks for low angles in anatase and rutile phases in titania nanopowders [18, 19].

3.3.1.1 Raman Results

In *figure* 3.1 we present the Raman spectra of sample A at different temperatures. Notice that the phase transition starts at approximately 700 °C and it is almost completed at 750 °C, what it is in good agreement with results found in literature for pure TiO_2 samples. As it is well known, the anatase metastable phase becomes rutile (stable) when it is submitted to temperatures above 700 °C [19, 20]. The phase transition is fast and takes a short temperature range to complete the total evolution from the metastable to the stable phase.

In *figure 3.2*, we show the Raman spectra corresponding to the phase transition evolution with temperature in sample B. In this case, the loading

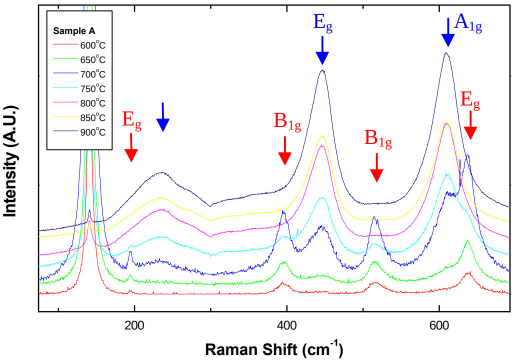

Figure 3.1. RAMAN spectra of sample A pure TiO_2 nanocrystals at various temperatures (600-900 °C). Notice the anatase-rutile transition when increasing the annealing temperature. Anatase and rutile main peaks are marked with red and blue arrows, respectively.

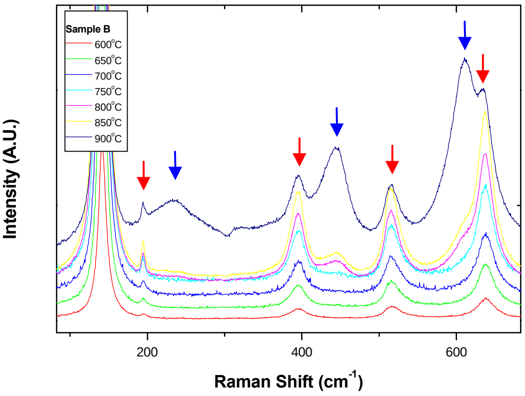

Figure 3.2. RAMAN spectra of sample B, low Nb loading, TiO_2 nanocrystals at various temperatures (600-900 °C). Notice the anatase-rutile transition when increasing the annealing temperature. Anatase and rutile main peaks are marked with red and blue arrows, respectively.

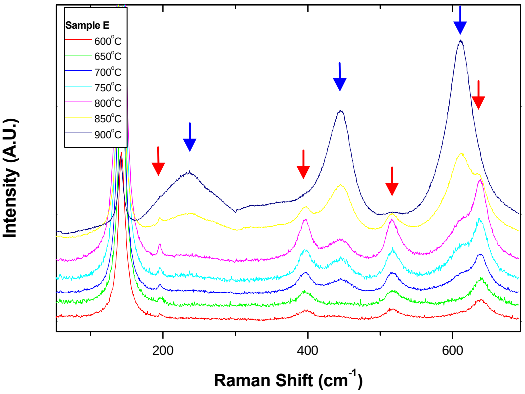

Figure 3.3. RAMAN spectra of sample E, high Nb loading, TiO_2 nanocrystals at various temperatures (600-900 °C). Notice the anatase-rutile transition when increasing the annealing temperature. Anatase and rutile main peaks are marked with red and blue arrows, respectively.

of Nb in low percentage has been found to dramatically influence in the behavior of the transition. We observe an important delay in the temperatures range until we reach the rutile stable phase in comparison with the results obtained in the case of pure TiO_2 (sample A). Phase transition starts now at approximately 800 °C, what indicates a delay of 100 °C with respect to the pure titania sample. Another point to emphasize is that even at temperatures as high as 900 °C we still have got an important presence of anatase in our sample, what indicates that phase transition is occurring late and moreover slowly.

The last sample we have considered is one of the highly loaded (sample E). It is noticeable that phase transition also starts at 700 °C, in the same range than the sample without Nb. Although the transition from anatase to rutile starts at low temperatures, the total evolution takes its time, and the process is slow. It is not until we reach the 900 °C when we can consider that the transition is almost completed (the anatase signal has totally disappeared).

3.3.1.2 XRD Results

Similar results have been obtained when analyzing the samples by XRD. In the case of sample A (*figure 3.4*), the XRD spectra shows that phase transition for pure TiO_2 samples starts around 700 °C, or even a bit before, while for annealing values over 750 °C the anatase phase signal hardly appears.

In the case of sample B (*figure 3.5*), we find that rutile signal starts to be noticeable at around 800 °C, and how, even at 900 °C it coexists with anatase.

Finally, sample E’s XRD spectra are shown in *figure 3.6*. Similarly to the results offered by Raman spectroscopy, we obtain that the phase transition starts at 700 °C, even a bit before, and that the presence of anatase phase extends up to high annealing temperatures, the complete phase transition is not reached until 900 °C.

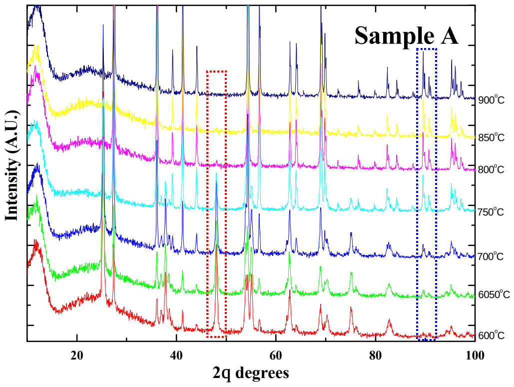

Figure 3.4. XRD spectra of sample A pure TiO_2 nanocrystals at various temperatures (600-900 °C). Notice the anatase-rutile transition when increasing the annealing temperature. Red and blue selections show the evolution of anatase and rutile peaks, respectively.

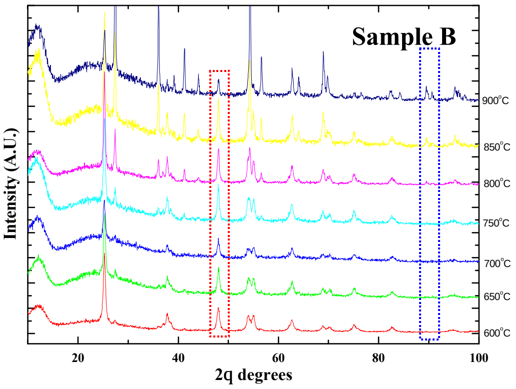

Figure 3.5. XRD spectra of sample B, low Nb loading, TiO_2 nanocrystals at various temperatures (600-900 °C). Notice that anatase-rutile transition when increasing the annealing temperature is highly slowed down. Red and blue selections show the evolution of anatase and rutile peaks, respectively.

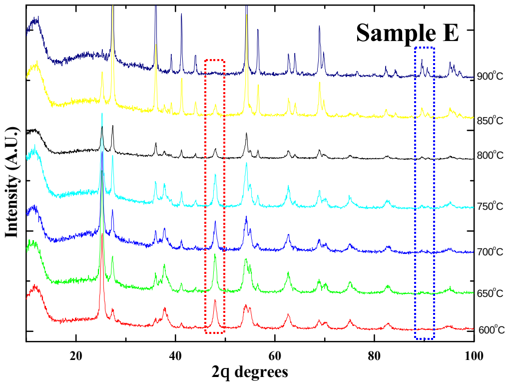

Figure 3.6. XRD spectra of sample E, high Nb loading, TiO_2 nanocrystals at various temperatures (600-900 °C). Notice the anatase-rutile transition when increasing the annealing temperature. Red and blue selections show the evolution of anatase and rutile peaks, respectively.

3.3.2 Influence of the Nb Loading Percentage

Once we have studied the evolution of the samples with the annealing temperature, we will analyze the evolution of the whole samples at a selected temperature, in order to strictly compare the effects attributed to the metal loading percentage.

3.3.2.1 Raman Results

In this way, we have obtained the Raman spectra of all the samples (A-E) at two interesting temperatures. The first set of spectra was obtained at 700 °C, temperature at which phase transition starts for pure TiO_2. The second annealing temperature analyzed is 900 °C, which gives information about the stabilization rate at high temperatures. One sample will be stabilized when all the material reaches the rutile stable phase. In the spectra presented, we have magnified the wavenumber range comprised between 350 and 550 cm^{-1}. This magnification allows us to observe the evolution of the most characteristic Raman-active modes for anatase and rutile, such as: two B_{1g} modes for anatase (at 397 and 516 cm^{-1} respectively) and an E_g mode in the case of rutile (at 449 cm^{-1}).

The evolution of the Raman-active modes of the samples treated at 700 °C is imaged in *figure 3.7*. At this temperature, we observe that phase transition has already started in pure TiO_2 sample (A) and in those with high Nb loadings (D and E), while in those samples with low Nb atomic percentage (B and C) the anatase phase signal is still the only one present.

The evolution of the Raman-active modes obtained at 900 °C is shown in *figure 3.8*. Notice that even at this high temperature the samples with low Nb atomic percentage (B and C) have an important percentage of anatase coexisting with the stable rutile phase. Another result to point out is that sample D and E show a similar behavior than A.

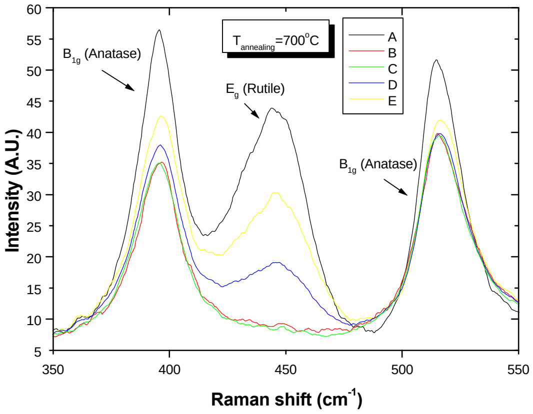

Figure 3.7. RAMAN spectra of samples A-E at 700 °C. The anatase-rutile phase transition occurs at different speed depending on Nb loading percentage.

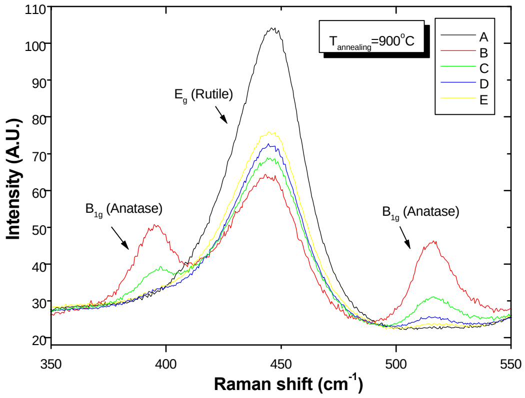

Figure 3.8. RAMAN spectra of samples A-E at 900 °C. Even at such high temperature, low Nb loaded samples (B and C) still have anatase phase coexisting with the stable rutile phase.

3.3.2.2 XRD Results

A similar experience has also been performed by using XRD. In this case, the phase transition evolution was analyzed at three different temperatures. At 600 °C, before the general start of phase anatase-rutile transition. At 750 °C, temperature at which the most important changes occur (for pure TiO_2 samples). And finally at 900 °C, the complete stabilization point for TiO_2. In every set of spectra we have selected a typical diffraction peak: the (200) in the case of anatase and the (111) for rutile, which have been marked in the *figures* presented in order to facilitate the observation of the temperature evolution.

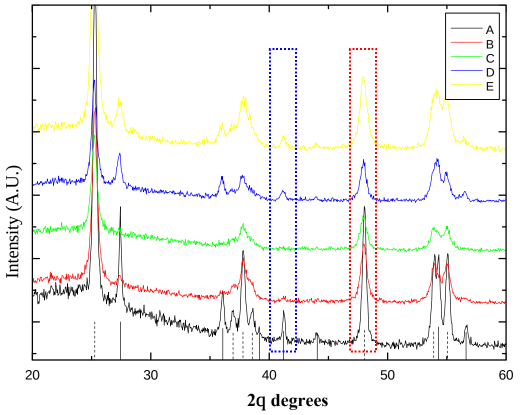

Figure 3.9. XRD spectra of samples A-E at 600 °C. The main part of TiO_2 nanoparticles are in their anatase phase. Red and blue selections show the evolution of anatase and rutile peaks, respectively.

$T_{calcination}$ = 600 °C
……………… TiO_2 Anatase
——— TiO_2 Rutile

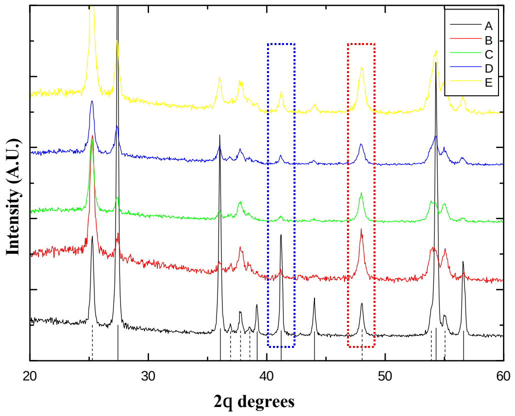

Figure 3.10. XRD spectra of samples A-E at 750 °C. This spectra corresponds to the usual transition temperature. Observe that low Nb loaded samples delay the phase transition. Red and blue selections show the evolution of anatase and rutile peaks, respectively.

$T_{calcination}$ = 750 °C
……………… TiO_2 Anatase
——— TiO_2 Rutile

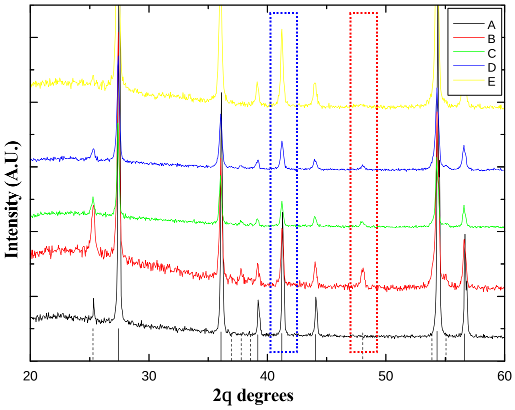

Figure 3.11. XRD spectra of samples A-E at 900 °C. Even at such high temperature, low Nb loaded samples (B and C) still have anatase phase coexisting with the stable rutile phase. Red and blue selections show the evolution of anatase and rutile peaks, respectively.

$T_{calcination}$ = 750 °C
……………… TiO_2 Anatase
——— TiO_2 Rutile

Results obtained at 600 °C are shown in *figure 3.9*. At such a low temperature the presence of rutile stable phase is observed in sample A in an appreciable proportion, while in D and E the rutile signal is weak. Samples B and C do not show any noticeable rutile peak.

At 750 °C, as shown in *figure 3.10*, the presence of rutile in samples A and E is important, and in D starts to grow. On the other hand, samples B and C continue mainly in their anatase phase, since the rutile peaks are still slightly visible.

Finally, when we reach the top annealing temperature (900 °C), as shown in *figure 3.11*, rutile stable phase is present in all samples. This phase is the dominant in samples A, D and E, however, in samples B and C it still coexists with an important proportion of anatase.

3.3.3 Anatase/Rutile Ratio Evolution

In the former *sections* we have presented a qualitative overview of the anatase to rutile phase transition analyzing the influence of temperature and Nb loading percentage. In the following, we have tried to obtain quantitative results from the Raman and XRD spectra. It is well known that a perfect quantification is always a difficult task due to the large amount of variables that can interfere in the calculus giving an erroneous result. In this way, we have extracted the quantitative results desired by using well-known formulas usually found in literature.

In order to determine phase transformations (anatase to rutile), Raman and XRD peak intensity ratios have been used. As R. J. González showed in his Ph.D. Thesis work [21], the intensity ratio of the 141 cm^{-1} anatase peak (I_{141}) to the 440 cm^{-1} rutile Raman peak (I_{440}) can be used to determine the phase composition. It that work, they used samples of known phase composition in order to calibrate the Raman spectra and the empirical result is shown below,

$$A/R = 0.038 \cdot \frac{I_{141}}{I_{440}} \tag{3.1}$$

where the small value for the numerical factor is a consequence of the great intensity of the 141 cm^{-1} anatase line.

Likewise, the ratio between anatase and rutile extracted from XRD spectra was computed with the empirical relation used by Depero et al. in one of their works [8],

$$R(T) = 0.679 \frac{I_R}{I_R + I_A} + 0.312 \left[\frac{I_R}{I_R + I_A} \right]^2 \tag{3.2}$$

where R(T) is the content of rutile in percentage at every temperature I_A is the intensity of the main anatase reflection (101) and I_R is the intensity of the main rutile reflection (110).

The main results obtained by applying both formulas to our Raman and XRD spectra are summarized in *figures 3.12* and *3.13*, respectively. Notice that in the case of the Raman data quantification, the points calculated, range from 750 °C to 900 °C. These are the most interesting points, since we start at the position in which the most important phase changes are occurring. Nevertheless, the phase transformations have been analyzed in the whole range of temperatures (from 600 °C to 900 °C) in the case of XRD.

The quantitative results offered by both methods show a similar behavior of the samples phase evolution. Notice that in both *figures* we have marked with an orange dashed line the point of the 50 % mixture, it means, the point at which both phases reach the same proportion in the sample (50 % of anatase and rutile). Comparing results, and considering this point as one of the most characteristic, we find that Sample A reaches the 50 % point at around 710 °C, and then it quickly evolve to a complete rutile transformation. At around 750 °C sample A have reached a 90 % of rutile transformation.

In the case of the low loaded samples (B and C) the 50 % rutile transformation do not occur until temperatures higher than 860 °C. And then even at temperatures as high as 900 °C, there is an important part of anatase still remaining in our samples, up to 25 % in the case of sample B and 20 % in the case of sample C.

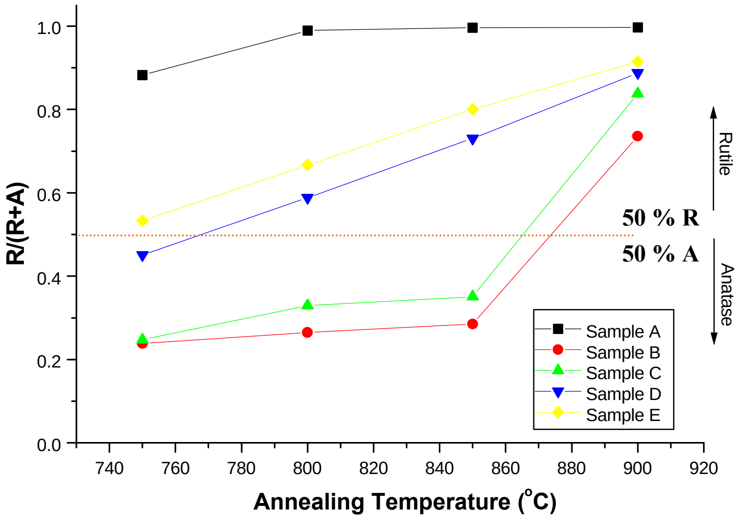

Figure 3.12. Anatase-Rutile phase transition evolution with temperature for samples A-E. Data obtained from RAMAN results using R. J. González (*Expression 3.1*).

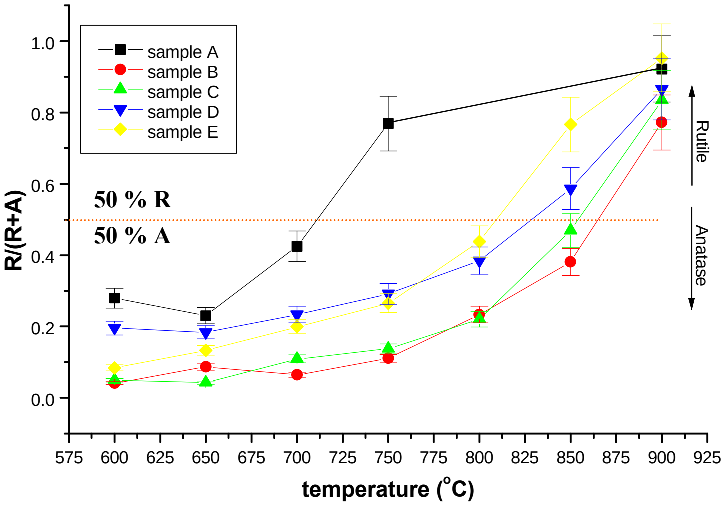

Figure 3.13. Anatase-Rutile phase transition evolution with temperature for samples A-E. Data obtained from XRD results using Depero et al. (*Expression 3.2*).

For samples D and E, the highly loaded, we find slight differences when comparing the results obtained by Raman and XRD. On one hand, when using the Raman adjustment we obtain that the 50 % mixture is obtained at 750 °C and 775 °C for samples E and D, respectively. While, on the other hand, the temperatures calculated when using the XRD adjustment are a bit higher, 805 and 825 °C, for samples E and D, respectively. Anyway, the evolutions of the phase transition showed from both techniques are quite similar, and that is just what we wanted to obtain. The difference of the numerical results offered from both techniques in the region of more variation could be due to the different origin of the empirical expressions used to compute them. The slight differences may come from the methods used in order to calibrate their respective equipment. Since the expressions used for calculus had a semi-empirical origin, those slight variations for numerical results can be accepted. Nevertheless, for high temperature values, both techniques coincide again with results, obtaining around an 85 % and 90 % of rutile transformation for samples D and E respectively.

All the numerical data showed above is summarized in *table 3.4*.

Sample	**50 % Point (ºC)**		**% R at 900 ºC (%)**	
	Raman	XRD	Raman	XRD
A	-----	710 ± 15	90	90
B	875 ± 15	858 ± 15	75	75
C	885 ± 15	870 ± 15	80	80
D	750 ± 15	825 ± 15	85	85
E	775 ± 15	805 ± 15	90	90

Table 3.4 Raman and XRD numerical values

3.3.4 Comparison with SAED results. NbO segregation?

In the following we will compare the main results obtained at low (600 °C) and high (900 °C) annealing temperatures by using XRD and Raman with the qualitative results obtained by SAED.

In *figure 3.14*, we show the SAED patterns for all the samples annealed at 600 °C. We identified the rings and spots present in our patterns in order to determine the crystal phase to which they correspond (results are all summarized in the tables included in *section 3.7* as an appendix of this *Chapter*). Notice that the rings and spots analyzed have been marked in the diffractograms following a color notation: red circles (TiO_2 anatase), green circles (TiO_2 rutile) and finally with yellow circles the NbO phase. The analyzed rings were in all cases the 4 or 5 more characteristics, understanding that the rest (corresponding to lower interplanar distances) can be attributed to the majority phase found.

In general, all the samples annealed at 600 °C, show clear anatase rings (labeled as 1-5 in every pattern). The results are in good agreement with the ones obtained by Raman and XRD, where at such a low temperature the majority phase is anatase. At this annealing temperature, rutile spots (A-D) are in general, weaker and less numerous than the anatase ones. However, in samples A600, D600 and E600 the spots corresponding to the rutile phase are a bit more numerous and more intense than those showed in the case of B600 and C600 samples. Until now, all the results coincide more or less with those expected. Nevertheless the existence of few diffuse spots that do not correspond to any of the former phases, made us think about the possibility of an extra phase related with the presence of Nb. After indexing those spots, we have compared the data obtained with those showed in the *JCPDS* XRD tables for the different Nb oxide phases as well as the known alloys composed by Nb and Ti. The crystal phases taken into account are those corresponding to: NbO [22], NbO_2 [23], β-NbO_2 [24], Nb_2O_5 [25] and $TiNb_2O_7$ [26]. After comparing data from indexed patterns with the possible phase found in *JCPDS tables*, we found that the diffuse spots are in good agreement with the NbO phase.

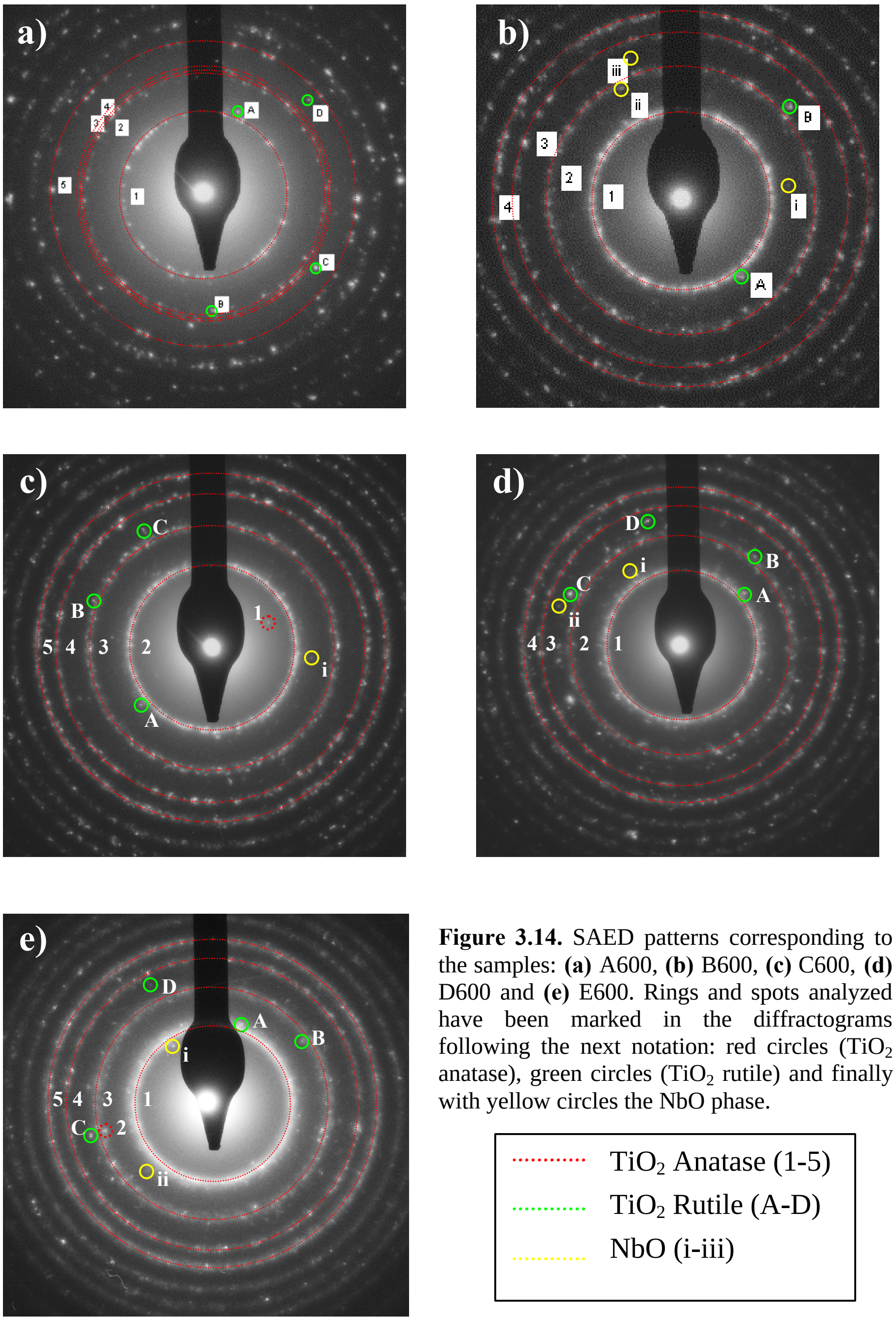

Figure 3.14. SAED patterns corresponding to the samples: **(a)** A600, **(b)** B600, **(c)** C600, **(d)** D600 and **(e)** E600. Rings and spots analyzed have been marked in the diffractograms following the next notation: red circles (TiO_2 anatase), green circles (TiO_2 rutile) and finally with yellow circles the NbO phase.

┈┈┈ TiO_2 Anatase (1-5)
┈┈┈ TiO_2 Rutile (A-D)
┈┈┈ NbO (i-iii)

The next set of samples analyzed using SAED was that corresponding to 900 °C annealings. In *figure 3.15*, we show the patterns obtained.

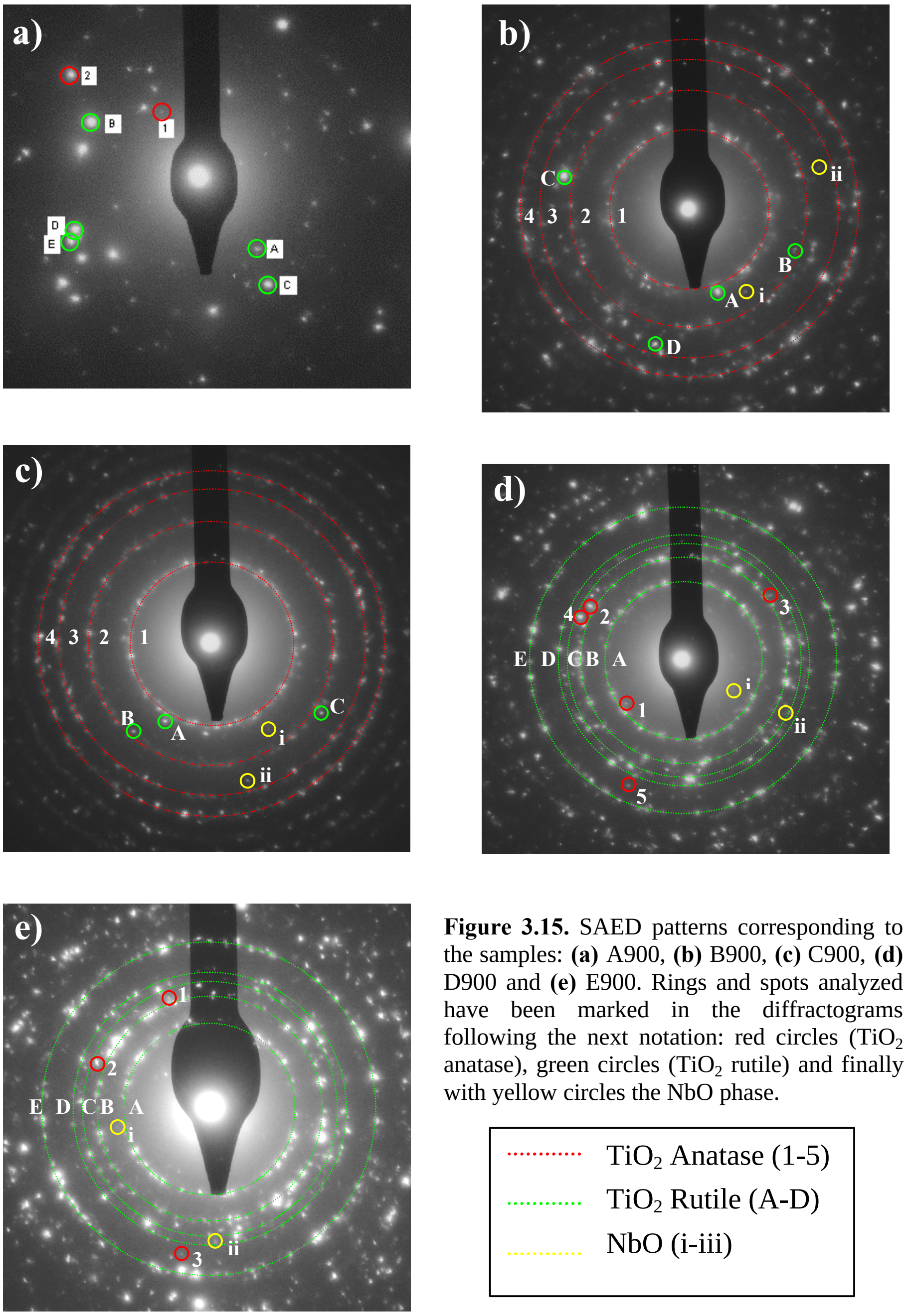

Figure 3.15. SAED patterns corresponding to the samples: **(a)** A900, **(b)** B900, **(c)** C900, **(d)** D900 and **(e)** E900. Rings and spots analyzed have been marked in the diffractograms following the next notation: red circles (TiO_2 anatase), green circles (TiO_2 rutile) and finally with yellow circles the NbO phase.

🟥 TiO_2 Anatase (1-5)
🟩 TiO_2 Rutile (A-D)
🟨 NbO (i-iii)

At this point it is interesting to point out that the presence of strong and wide spots, is due to the important grain size increment of the TiO_2 nanopowders at such a high temperature. That is the case of sample A900 pattern, and in lower proportion of samples D900 and E900. Another important characteristic that have changed with respect to the 600 °C patterns is that the majority phase is clearly rutile in samples A900, D900 and E900. However, the SAED patterns corresponding to B900 and C900 still have an important remaining of anatase. NbO diffuse spots can also be seen in these samples.

After SAED analysis, we can conclude that the phase transition evolution has been delayed in those samples with low Nb loading. Moreover, there has been an increase of the TiO_2 grain size at higher temperatures, since the rings are not so fine and continues, and several strong spots appear in the corresponding phase positions. Furthermore, the presence of NbO related diffuse spots suggest that there are metal oxide nanoclusters coexisting with TiO_2 grains.

We have to point out that no quantification has been made over SAED patterns since in order to obtain the spectra, just few hundreds of TiO_2 nanoparticles have been taken into account. In this way the quantification performed by XRD or Raman shows better results due to the most statistical features (the spectra is taken from a bigger amount of material). With SAED patterns we just wanted to obtain the phase composition of the samples studied, and to confirm the clear transition phase evolution. However, there is a good advantage when using SAED, and it is that we can easily find the presence of minor phases, since their signal is not buried when integrating the strong signal coming from majority phases.

Until now, we have presented the script of the effects that occur in our samples, but some specific questions are still unresolved:

- Why is there a delay in TiO_2 phase transition for low loaded samples?
- What is the origin of Niobium oxide signal in SAED patterns?

These questions can not be answered just from results presented until now. We will need to use nanoscopic techniques such as TEM and

HRTEM in order to study the nanostructural changes occurred in the samples. In this way, in the next *section*, we have performed a detailed analysis of the samples growth mechanisms in order to find the answer to the questions formulated above.

3.4 Growth Mechanisms in the Nb/TiO_2 System

In this *section*, a detailed study of the growth mechanisms of the samples loaded with different Nb percentage has been performed. In a first approach and using conventional bright field TEM techniques, we have determined the TiO_2 grain size of the samples annealed at low (600 °C) and high (900 °C) temperatures, analyzing the influence of the Nb loading (*Section 3.4.1*). Afterwards, we will use HRTEM associated techniques to analyze the evolution of the sample nanostructure, observing the effects of coalescence, metal segregation, phase transition, etc (*Section 3.4.2*).

3.4.1 Analysis of the TiO_2 Grain Size Evolution

3.4.1.1 Low Annealing Temperature (600 ºC)

In *figure 3.16*, we show a general bright field TEM view of all samples nanopowders after annealing at 600 °C. Notice the small grain size of all of them. No significant changes can be appreciated with the Nb loading percentage. In *figure 3.17*, the grain size histograms obtained from TEM micrographs are shown, results are all summarized in *table 3.5*. At such a low temperature, there is just a slight decreasing of nanoparticles size when increasing the metal loading value. The main contribution to grain size is due to the anatase nanograins, since Raman, XRD and SAED showed a majority presence of this phase in the samples at 600 °C. With this technique, we are not able to distinguish between anatase and rutile TiO_2 grains when measuring their size. However, there can not be big differences between both phases grain sizes, since it is not possible to distinguish two different distributions in our histograms.

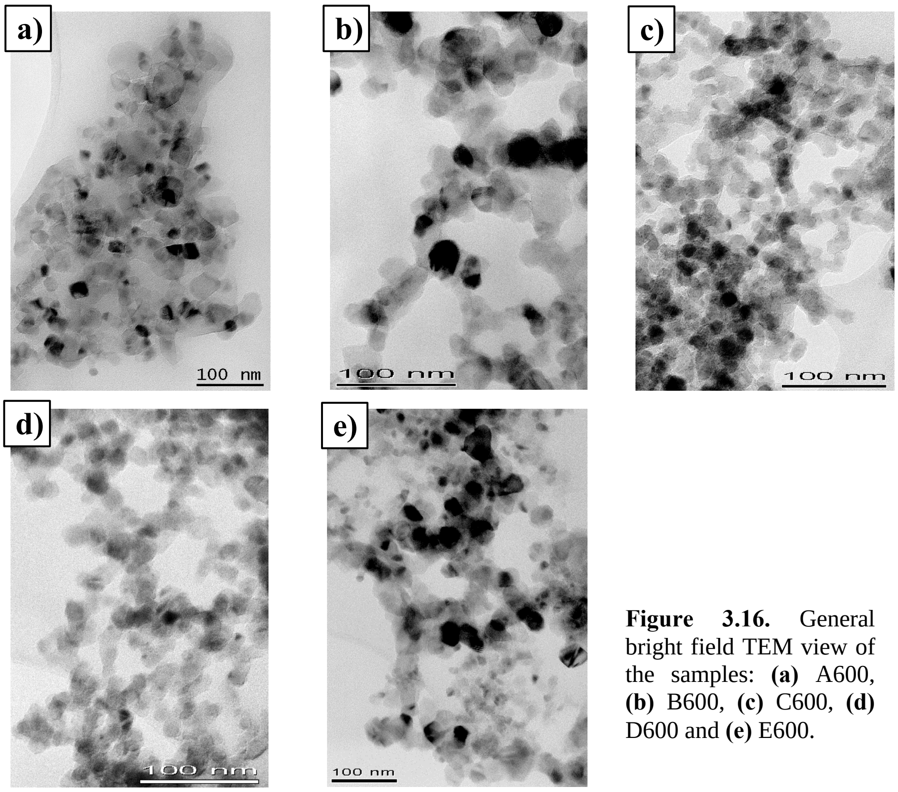

Figure 3.16. General bright field TEM view of the samples: **(a)** A600, **(b)** B600, **(c)** C600, **(d)** D600 and **(e)** E600.

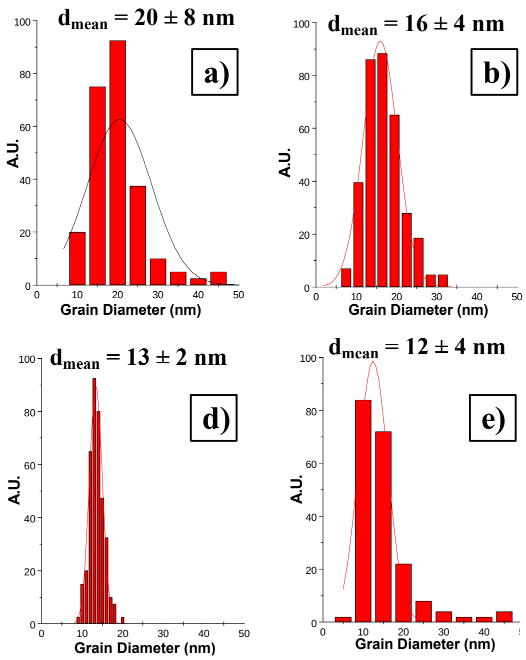

Figure 3.17. Grain size histograms corresponding to the samples: **(a)** A600, **(b)** B600, **(c)** C600, **(d)** D600 and **(e)** E600.

A600 d (nm)	B600 d (nm)	C600 d (nm)	D600 d (nm)	E600 d (nm)
20 ± 8	16 ± 4	14 ± 3	13 ± 2	12 ± 4

Table 3.5 Nanopowders mean diameter obtained from grain size histograms after gaussian fit.

3.4.1.2 High Annealing Temperature (900 ºC)

In the following, we have analyzed the grain size evolution of our samples at high temperature (900 °C). In *figure 3.18*, a set of TEM bright field micrographs corresponding to the different Nb loading percentages is shown. Their respective grain size histograms are also provided in *figure 3.19*. From the statistic results computed from the histograms, we observe a noticeable change of the grain sizes when increasing the loading values. All mean grain size results are summarized in *table 3.6*.

A900 d (nm)	B900 d (nm)	C900 d (nm)	D900 d (nm)	E900 d (nm)
130 ± 50	38 ± 10	32 ± 6	40 ± 10	57 ± 20

Table 3.6 Nanopowders mean diameter obtained from grain size histograms after gaussian fit.

3.4.1.3 General View

In order to visualize and compare all data obtained for mean grain size, we have built a graphic containing all data (*figure 3.20*). In this *figure*, we can appreciate the slight decreasing in samples grain size when increasing the Nb loading value at 600 °C. However, at 900 °C, the evolution of particles size is a bit different. The bigger nanoparticles are those corresponding to the unloaded sample A900. A dramatic decrease in particle size occurs when loading our samples with a low percentage of Nb. The particles mean size have a minimum value at around 2-3 % Nb atomic percentage, and then slowly increases when increasing the Nb loading. Notice that in samples A900, D900 and E900, anatase phase nanoparticles

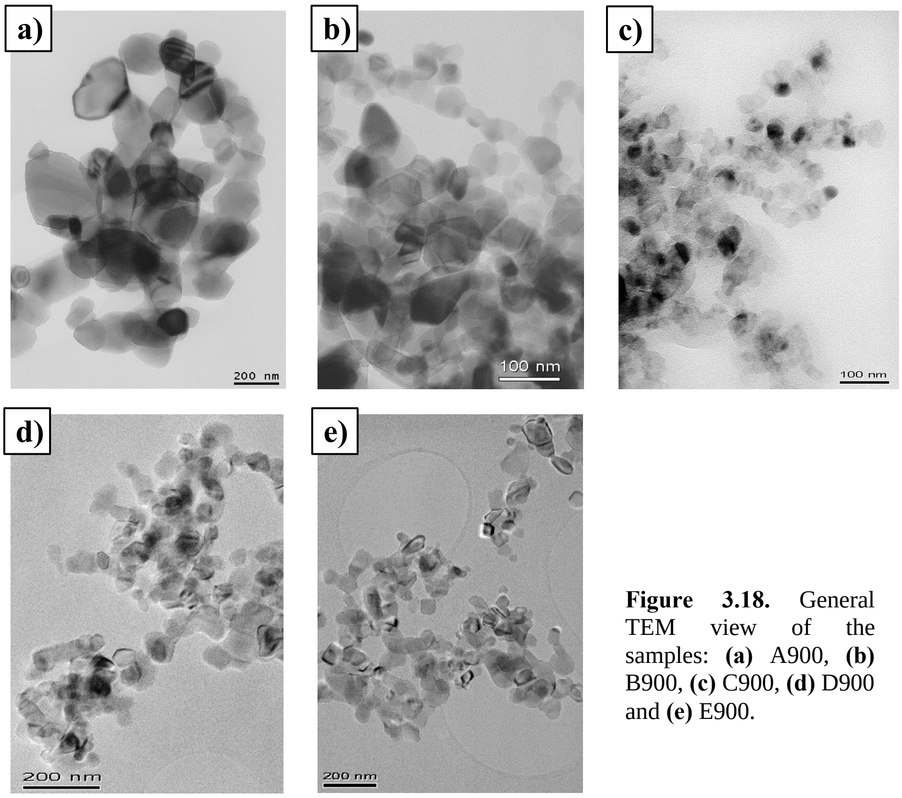

Figure 3.18. General TEM view of the samples: **(a)** A900, **(b)** B900, **(c)** C900, **(d)** D900 and **(e)** E900.

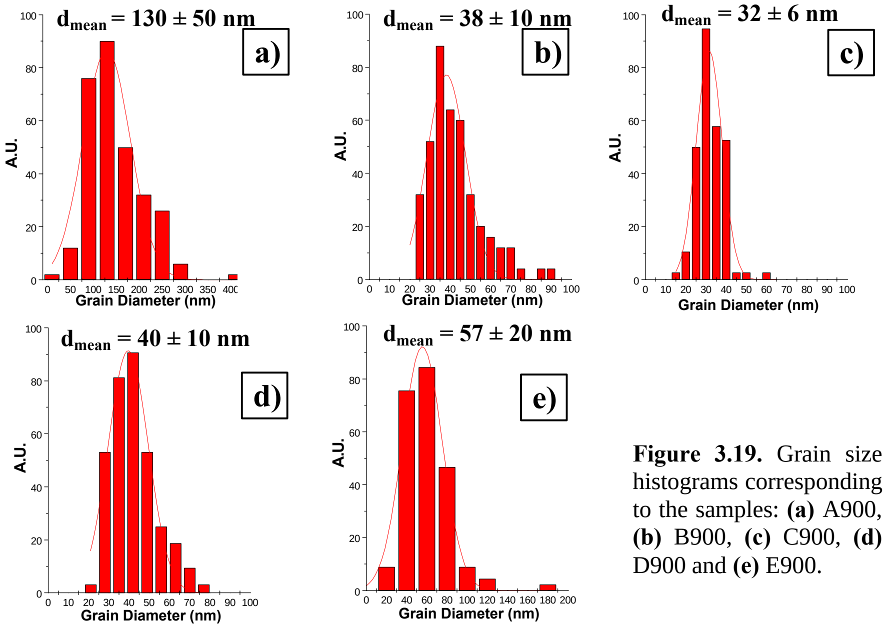

Figure 3.19. Grain size histograms corresponding to the samples: **(a)** A900, **(b)** B900, **(c)** C900, **(d)** D900 and **(e)** E900.

do almost not contribute to the statistics, since anatase phase was hardly detected by the spectroscopic techniques used in the former *section* at such a high temperature. On the other hand, anatase phase nanoparticles are expected to contribute in statistics for samples B900 and C900, as anatase phase has been shown to coexist with rutile (in an appreciable percentage, 20-25%) for such low loading values. After these observations, it is important to notice that the mean grain size is closely related with the presence of high or low quantities of rutile in the samples. In general, the most rutile we find in our samples, the bigger is the mean grain size.

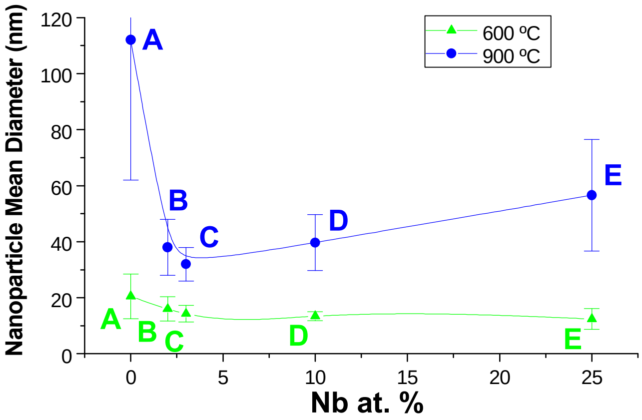

Figure 3.20. Grain size evolution at low (600 °C) and high (900 °C) annealing temperatures.

In the following, a complete HRTEM analysis has been performed, in order to study the morphological and nanostructural changes occurred during phase transition process.

3.4.2 Nanostructural Characterization

3.4.2.1 Unloaded Sample (no Nb added)

In *figure 3.21* we show a HRTEM micrograph of the sample A600. We show an example of two TiO_2 nanoparticles. DIP of the marked areas has been carried out. We find that the visible planes are characteristic of the anatase metastable phase. After HRTEM results, we realize that there is an important proportion of anatase phase nanoparticles although rutile particles is also present in lower percentage (in good agreement with the previous experimental results showed in *Section 3.3*).

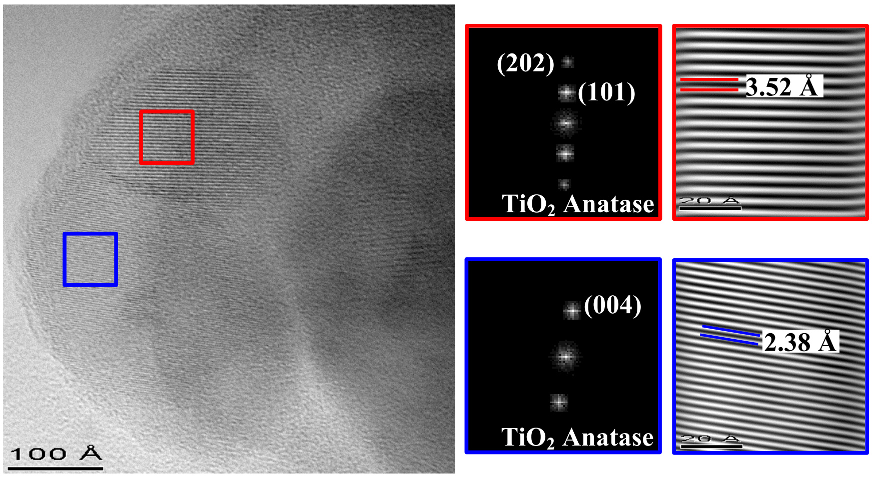

Figure 3.21. HRTEM micrograph showing the typical anatase nanograins observed at low annealing temperatures (600 °C, *sample A600*). DIP of the squared areas in blue and red are also enclosed on the right.

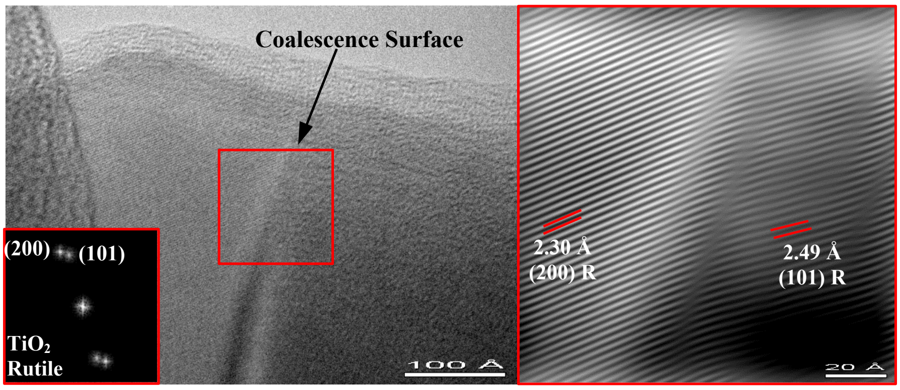

Figure 3.22. HRTEM detail of a TiO_2 rutile nanograin. Rutile grains are bigger than those found in the anatase phase in *sample A900*. Coalescence effects are present in the biggest rutile particles. DIP of the coalescence surface is also provided.

A dramatic change has been observed when analyzing the sample annealed at 900 °C. In this case the main part of the particles have crystallized in the stable rutile phase. In *figure 3.22*, we show an example of a TiO_2 rutile nanoparticle that is the result of the coalescence between two other. The different family planes found after DIP, show that both parts of the sample have crystallized with different orientations. Effects of coalescence between TiO_2 can be one of the reasons for the fast growth of TiO_2 nanoparticles at such a high temperature.

3.4.2.2 Low Nb Loaded Samples

An example of sample B600 nanoparticles is shown in *figure 3.23*. The main part of the TiO_2 grains is in the anatase phase, as shown in the

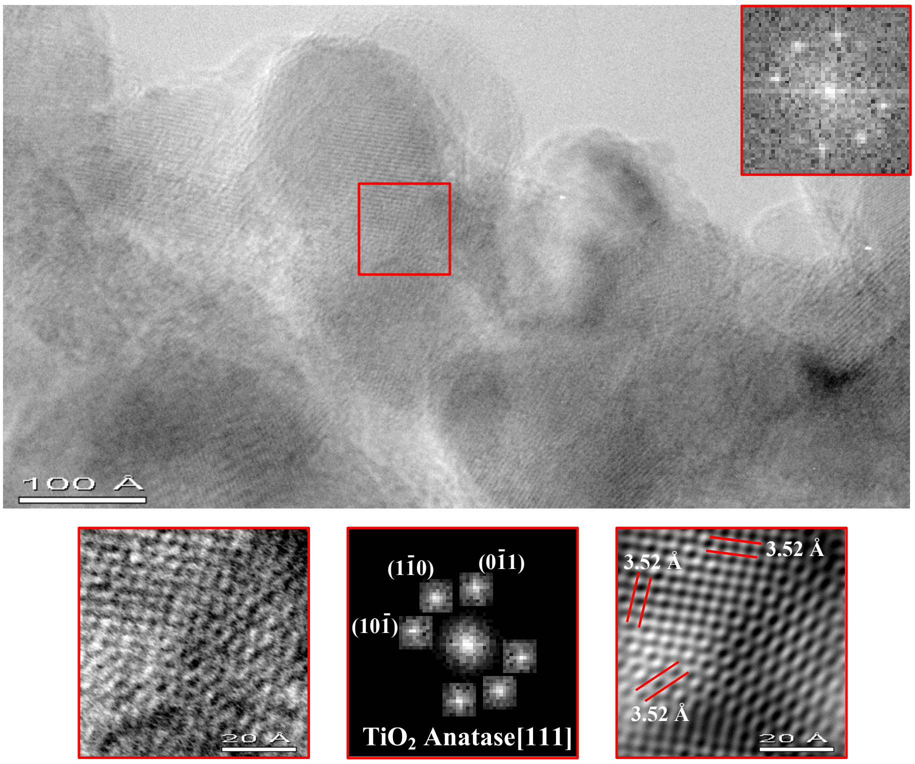

Figure 3.23. HRTEM micrograph showing some anatase particles in sample B600. DIP of the squared area in red is also enclosed. The detail selected corresponds to the anatase phase imaged in the [111] zone axis.

HRTEM micrograph. Notice that for low loaded samples at such a low temperature, the proportion of anatase versus rutile is high, although there are also few rutile nanoparticles coexisting with the anatase ones. An example of this coexistence is shown in *figure 3.24*, corresponding to sample C600. In this case, a TiO_2 rutile nanoparticle has been found next to several anatase grains. We have also analyzed the presence of small nanoclusters on TiO_2 grains (see as an example the detail squared in red in *figure 3.24*). Further analysis have showed that the clusters are composed by Nb oxidized species mainly NbO.

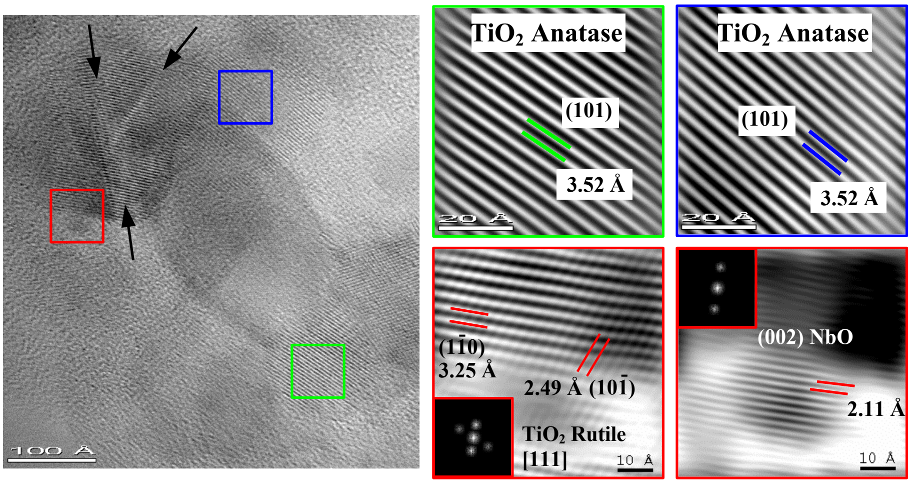

Figure 3.24. HRTEM micrograph showing sample C600 nanopowders. The main part of nanoparticles is in the TiO_2 anatase phase. Details squared in blue and green correspond to anatase particles as shown in their DIP on the right side. Detail squared in red corresponds to a TiO_2 rutile nanograin with a segregated NbO nanocluster on its surface, as DIP analysis show on the right side. Black arrows mark the presence of dislocations in the TiO_2 nanoparticle.

At high annealing temperatures, the quantity of TiO_2 rutile nanoparticles increases substantially, however, in less proportion than for unloaded samples. In *figure 3.25*, we show an example of the coexistence of rutile and anatase crystal phases. A high number of nanoparticles are decorated with nanoclusters. The small nanoclusters (around 2 nm of diameter) are composed of NbO, as determined after DIP of the HRTEM micrographs. An example of this NbO nanoclusters presence is shown in *figure 3.26* where a plan view example has been analyzed. From a plan view HRTEM image is impossible to determine if the nanoclusters observed are placed on TiO_2 grains surface or if they are included inside TiO_2 matrix.

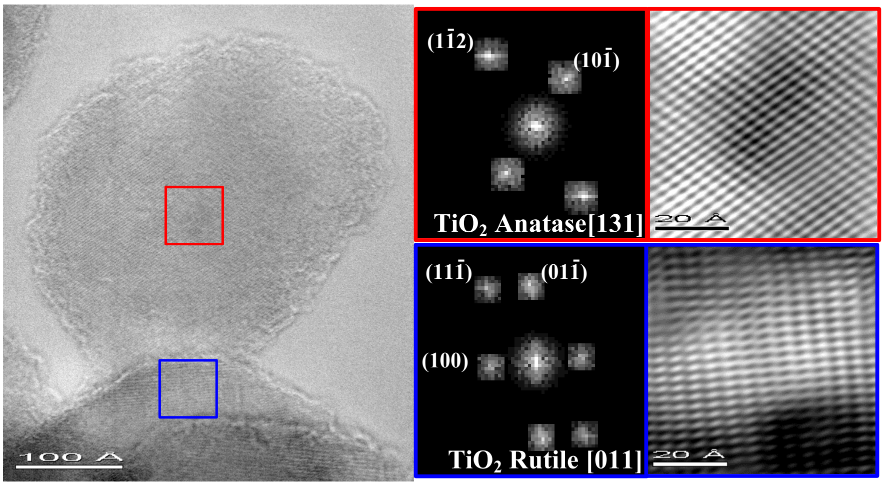

Figure 3.25. HRTEM micrograph of B900 sample. We show the coexistence of anatase nanoparticles with the rutile ones. DIP of both selected areas is provided on the right side.

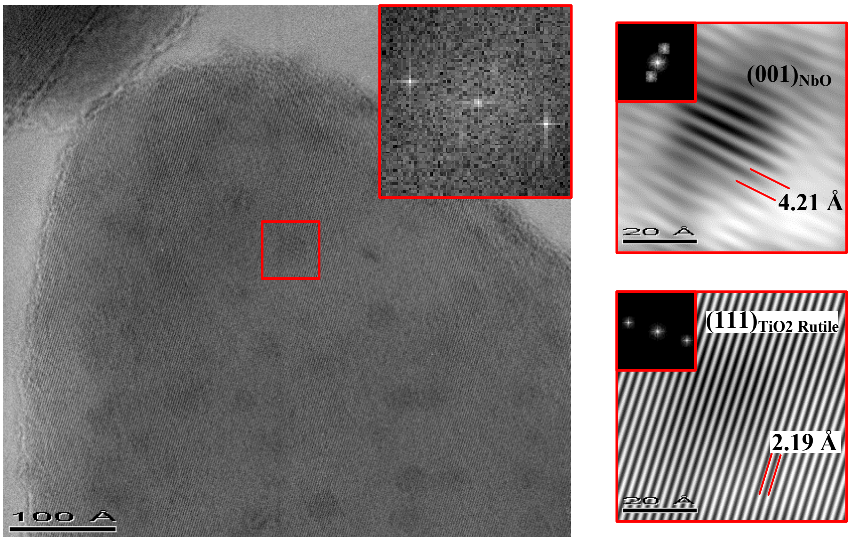

Figure 3.26. HRTEM micrograph of sample B900. Some NbO nanoclusters are segregated on TiO_2 rutile nanoparticles surface (in dark contrast). We provide the DIP analysis of one of these nanoclusters in plan view, on the right side, extracting NbO information from rutile background.

In this way, it is important to analyze HRTEM profile view images, as that shown in *figure 3.27*, where we can observe that the NbO clusters are clearly placed on TiO_2 nanoparticles surface. At this point, it is interesting to point out that all the NbO nanoclusters that we have found, have been always placed on TiO_2 rutile nanoparticles surface, and never on anatase nanoparticles.

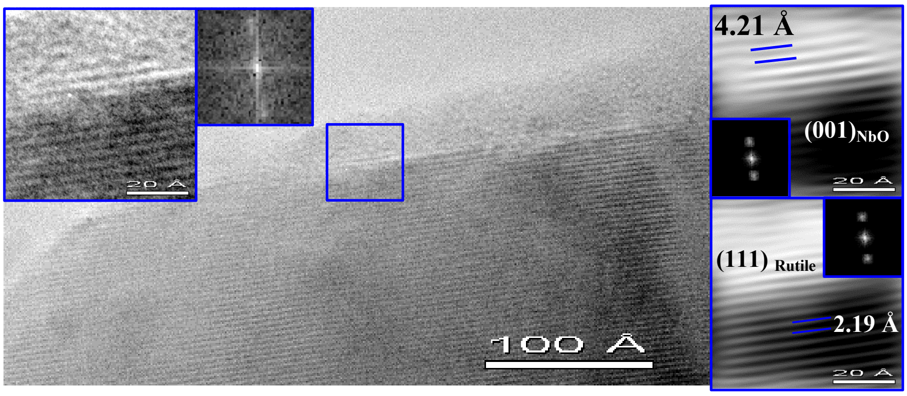

Figure 3.27. HRTEM micrograph showing a profile view NbO aggregate on a TiO_2 rutile nanoparticle surface (*sample B900*). DIP analysis is also enclosed.

3.4.2.3 High Nb Loaded Samples

Samples D600 and E600, which have been loaded with a high percentage of Nb, have got the main part of the TiO_2 crystallized in the anatase phase. In this case the percentage of anatase is higher than that obtained for the unloaded samples, while it is lower than the obtained for low Nb loadings, as found after spectroscopic analysis made in *Section 3.3*, and also as the HRTEM measurements corroborates. In this way, we show an example of few TiO_2 nanoparticles from sample E600, finding the common presence of anatase, as expected (*figure 3.28*).

When increasing the temperature, we have found that the percentage of rutile phase nanoparticles increases with respect to the anatase ones, in higher proportion than for low Nb loaded but lower than for the unloaded ones. As we have a big amount of rutile nanoparticles in these samples, it should be easier to confirm the previous results about Nb segregation as

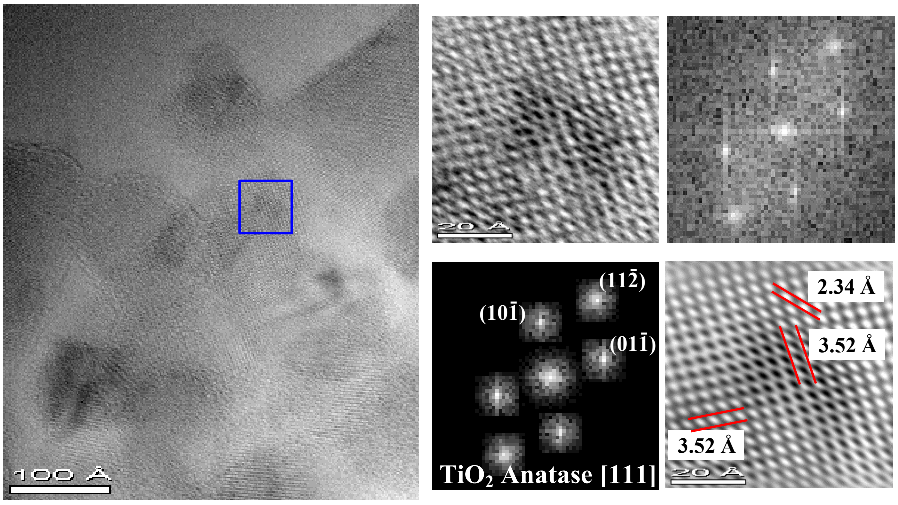

Figure 3.28. HRTEM micrograph showing sample E600 nanopowders. DIP of the squared area confirms the anatase structure of TiO_2 nanoparticles.

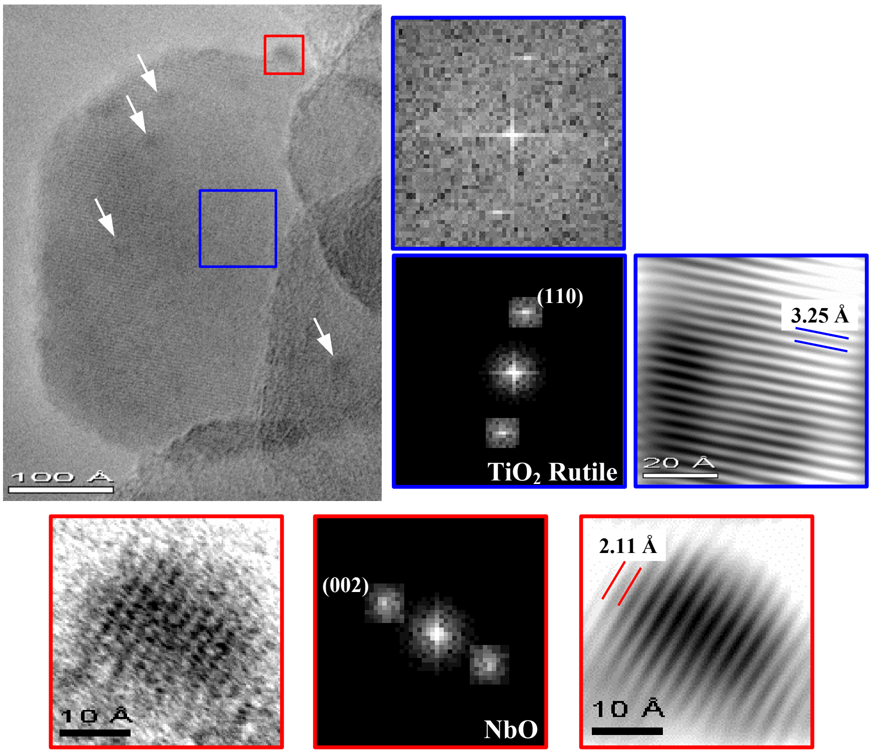

Figure 3.29. HRTEM micrograph of D900 sample. White arrows mark some of the NbO nanoclusters segregated on TiO_2 rutile surface. Squared in blue, a detail and its respective DIP of the rutile planes. In red, we show the DIP analysis of a NbO nanocluster.

oxidized nanoclusters. In *figure 3.29*, we show a typical TiO_2 rutile grain (from sample D900) decorated with several clusters, viewed in dark contrast. The analysis by DIP of one of the nanoclusters confirms its NbO structure.

In *figure 3.30*, an example of the highest Nb loading is shown (Sample E900). After DIP we confirmed that the big nanoparticle is in the rutile phase. Moreover, we have analyzed the small nanoparticle attached to its surface (squared in red), finding that it is in the TiO_2 anatase phase. In

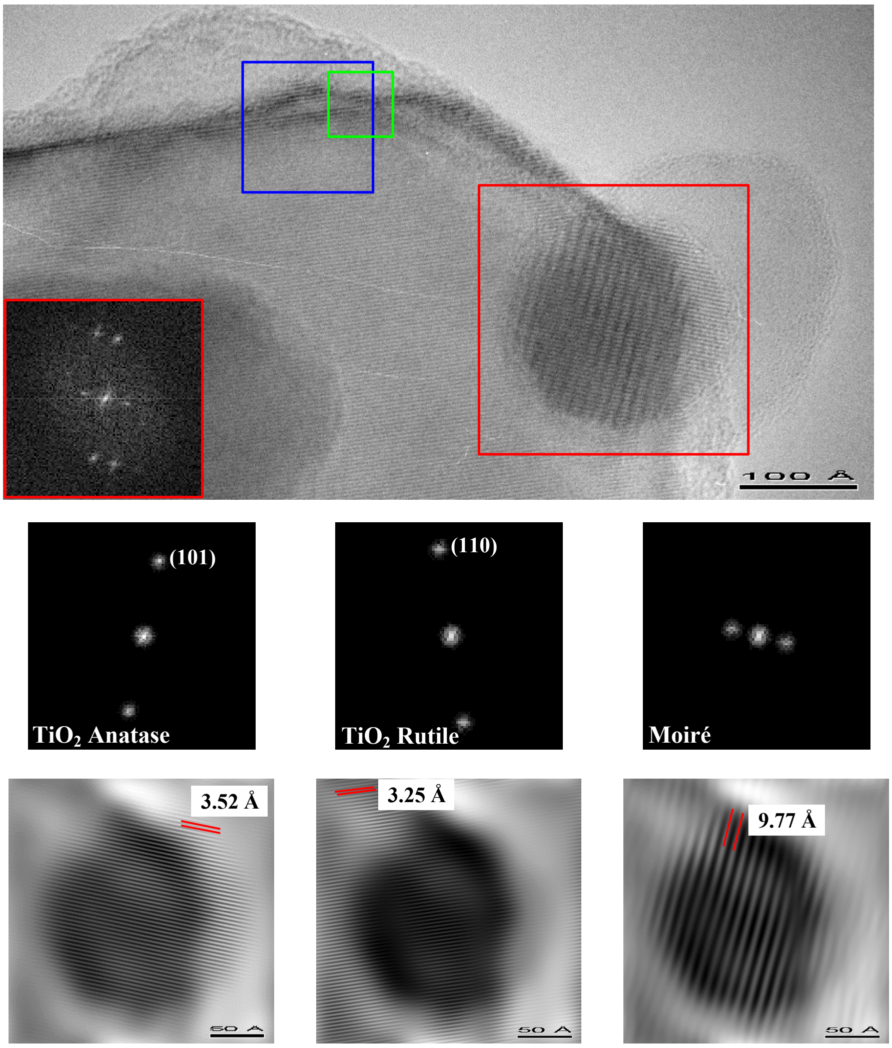

Figure 3.30. HRTEM micrograph of E900 sample. Selected area squared in red has been analyzed by using DIP. We have found that the small nanoparticle is still in the anatase phase, while the big one is already in rutile.

this case, no NbO clusters are appreciated on surface. It is also interesting to analyze the different contrast patterns observed in TiO_2 rutile particle borders.

In *figure 3.31* we have studied the area marked in blue in *figure 3.30*. The digital diffractogram of the image shows the coexistence of three different phases: TiO_2 rutile, TiO_2 anatase, and NbO. Applying a mask filter to the diffractogram and obtaining the inverse FFT, we could obtain the

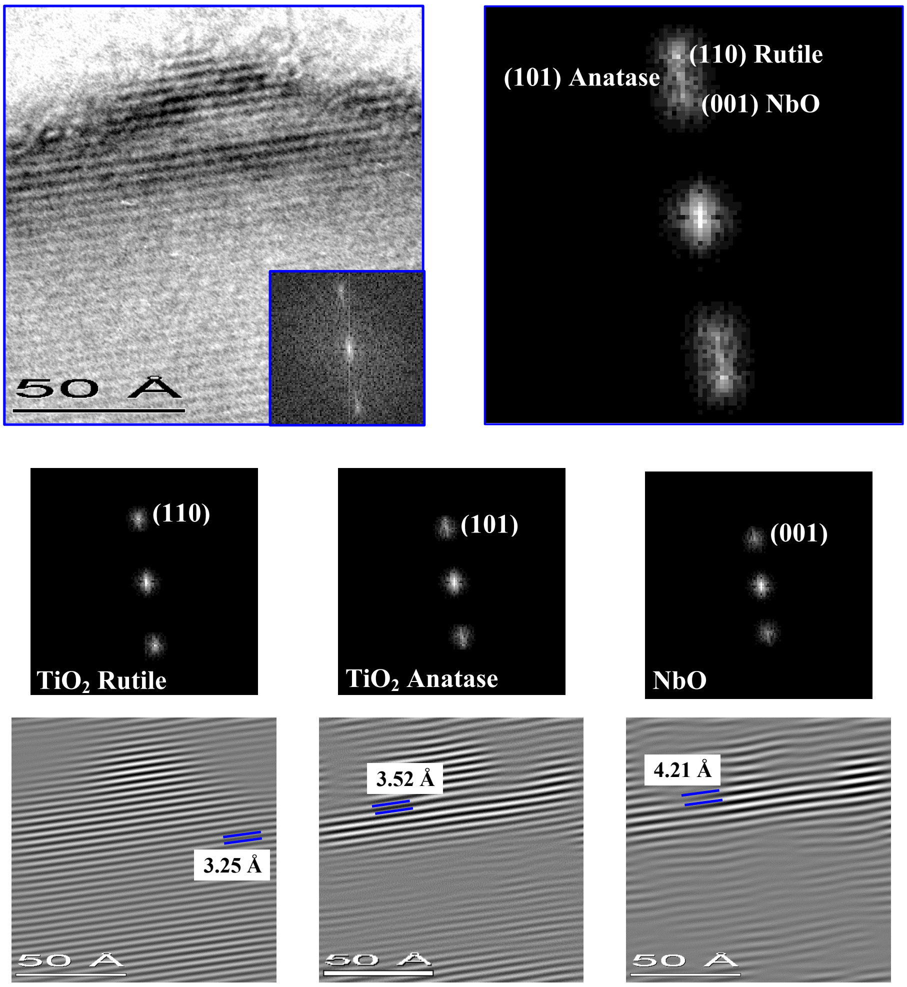

Figure 3.31. HRTEM micrograph of E900 sample. In this *figure* we provide the DIP of the selected area squared in blue in *figure 3.32*. The main part of the nanoparticle is formed by TiO_2 rutile phase, however, particle surface is covered by few monolayers of TiO_2 anatase and emerged NbO.

distribution of these phases. The particle bulk, seems to be composed of TiO_2 in rutile phase (what it was expected), while few monolayers of NbO and anatase can be also distinguished on particle surface.

In *figure 3.32*, we have analyzed the area squared in green in *figure 3.30*. In this case, on the top surface of the TiO_2 rutile there is NbO, as shown after DIP. This means that the anatase thin film covering the grain is not continuous, and that in some areas, the nanoparticle reached the complete phase transformation.

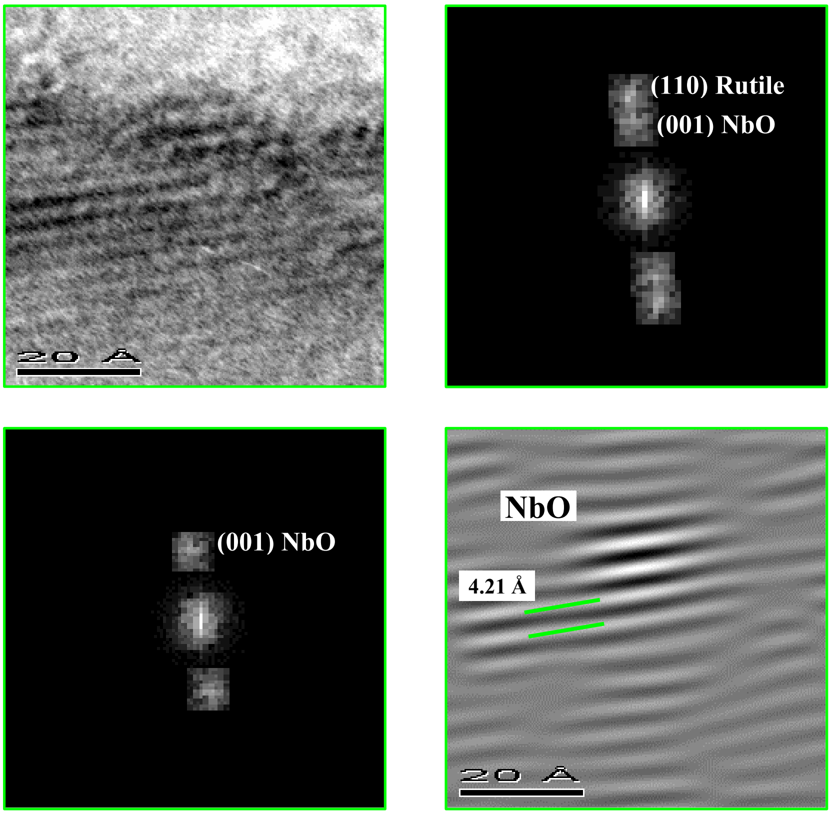

Figure 3.32. HRTEM micrograph of E900 sample. In this *figure* we provide the DIP of the selected area squared in green in *figure 3.32*. Notice the presence of NbO nanoclusters on the NbO monolayers placed on TiO_2 rutile nanoparticle.

After HRTEM results presentation, few more questions have appeared to be unresolved:

- Is there any relation between Niobium Oxide and TiO_2 phase transition?
- Why is there no Niobium on TiO_2 anatase particles surface?
- Why is there an anatase and rutile thin film disposition on some TiO_2 rutile nanoparticles at high annealing temperatures?
- Which is the phase transition mechanism?

In order to find the possible answer to all these questions, in the following *Section* we are going to discuss all the results obtained until now, comparing the different techniques used.

3.5 Discussion about Experimental Results

3.5.1 Anatase to Rutile Transition Modeling

The results obtained for low loaded samples where oxidized Nb formed small nanoclusters on the surface of the TiO_2 rutile nanoparticles, make us think about the reason of this phenomena, and why there is no presence of this clusters on any of the anatase grains analyzed. In order to solve the unknown, we have selected an apparently “clean” anatase TiO_2 nanoparticle and we have obtained an EDS spectrum of it (as shown in *figures 3.33.a* and *b*). The spectrum obtained reveals the presence of Nb related signal coming from the particle. As no clusters have been observed next to it, we suggest that Nb atoms could be placed inside TiO_2 anatase bulk.

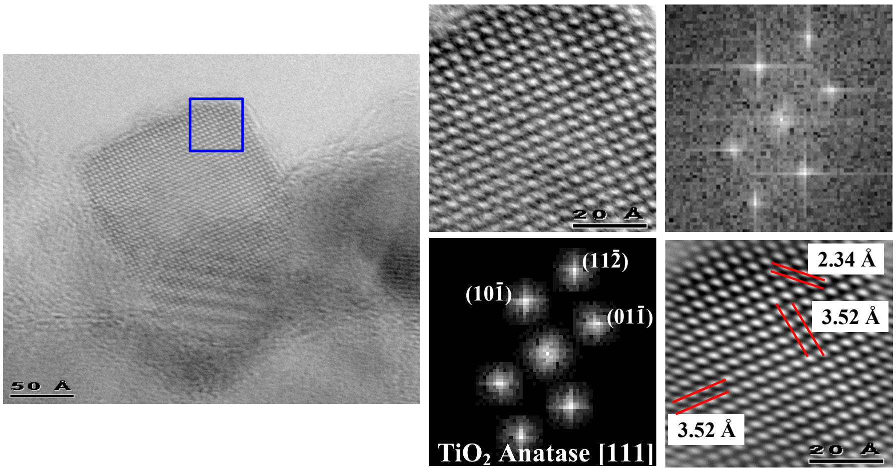

Figure 3.33.a. HRTEM micrograph showing sample D600 nanopowders. In the image we show a rectangular shape anatase nanoparticle. DIP is provided on the right side, allowing us to determine the atomic structure of the selected grain.

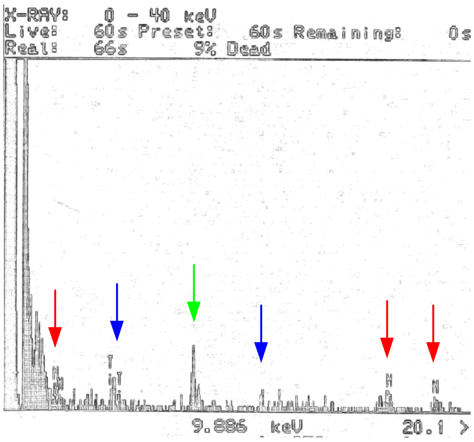

Figure 3.33.b. EDS spectrum corresponding to the area shown in *figure 6.23.a.* The presence of Nb atoms (red arrows) is evident although the signal is weak. Titanium also presents two peaks (blue arrows). While Cu is also present (green arrow), this last signal comes from X-ray scattered in the copper grid.

Moreover, according to the disposition of anatase and NbO thin layers found by HRTEM in *figure 3.31*, we have essayed different possibilities, and we finally present a possible model (*figure 3.34.a*). The suggested model has been reproduced by using a complex supercell. In this model, we have taken into account a pure TiO_2 rutile particle's bulk covered by few monolayers of NbO, with a thin anatase film on the top. The model suggests a phase transition occurring from inside to outside of the nanoparticle. When anatase is transformed to rutile, the Niobium atoms would be segregated outside the rutile stable phase creating in this case a thin NbO film (in the case of high Nb loadings) or small nanoclusters (in the case of lower Nb loadings). Moreover, the anatase layers from the exterior surface (still containing Nb atoms in their structure) would not have had time to transform into rutile, the example shown is like a freeze picture of the phase transformation. It is normally expected that phase transition is fast enough for not to be observed, and that is what we usually find in our samples (or rutile, or anatase nanoparticles, but never mixed phases in a same grain). Nevertheless, we have been lucky in this occasion due to the low probability of finding a nanoparticle in such a freeze situation, which highly contributes to the comprehension of the phase transition phenomena.

In order to confirm the results, we have simulated the model obtaining similar contrast patterns and the same plane spacing distances when comparing the HRTEM simulated image with the one obtained experimentally (*figures 3.34.b and 3.34.c*, respectively). This similarity between the proposed model and the experimental image make us think that the suggested model may be close to reality.

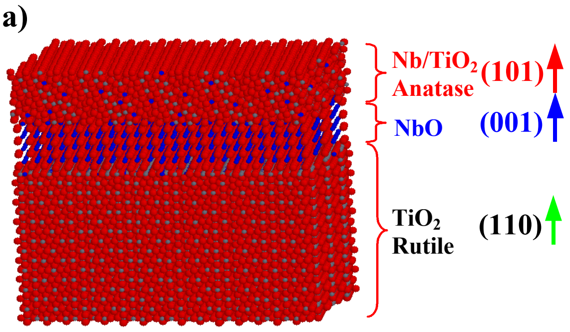

Figure 3.34. a) Supercell model reproducing the growth mechanism shown in *figure 3.32*. Phase transition occurs from inside to outside at the same time that Nb is segregated from anatase when this is transformed into rutile. **b)** CIS of the model shown in **(a)**, notice the good resemblance of contrast lines with those shown in the HRTEM micrograph in **(c)**.

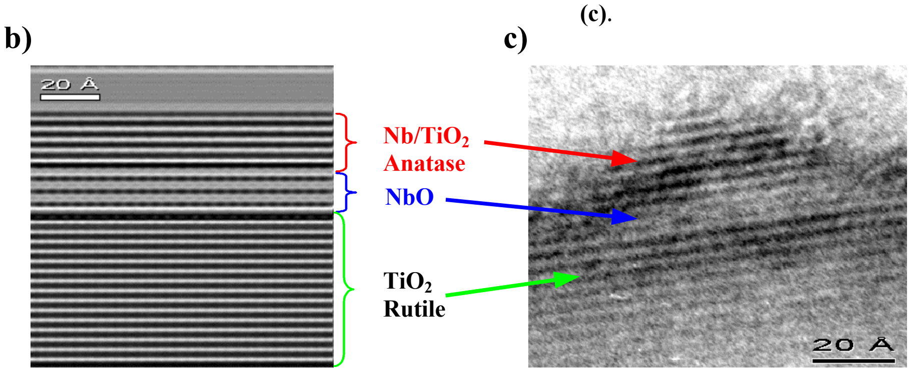

Once the transition model has been proposed, we are going to discuss the reasons of this Nb segregation and the grain growth and phase transition hindering before transformation.

3.5.2 Background

The coordination of Ti is 6-fold in both anatase and rutile but the octahedral sites in anatase are highly distorted (see *figures 3.35.a* and *3.35.b* for the anatase and rutile octahedral models, respectively). The defect structure of TiO_2 is very complex; the various point defects for which evidence exists in anatase are oxygen vacancies, interstitial or substitutional Ti^{3+} ions, and interstitial Ti^{4+} ions. During the phase transformation, the anatase pseudo-close-packed planes of oxygen {112} are retained as the rutile close-packed planes {110} and a cooperative rearrangement of the titanium and oxygen ions occur within this configuration [27]. The oxygen vacancies placed in anatase planes act as nucleation sites for the anatase to rutile phase transformation [28].

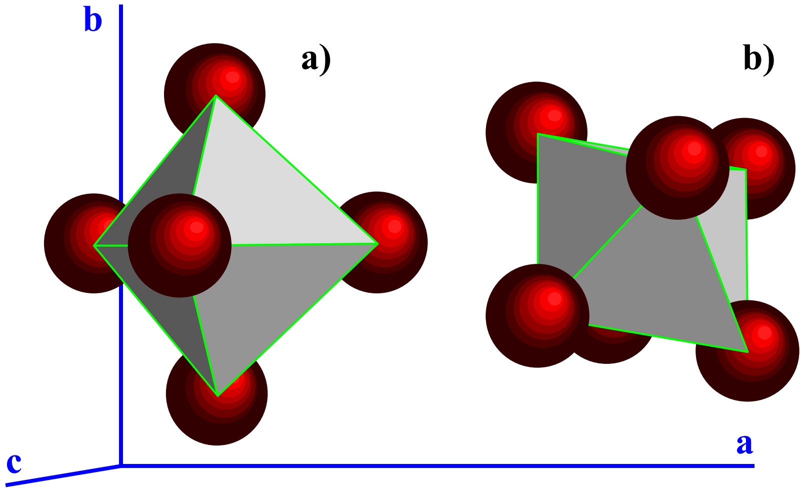

Figure 3.35. a) Anatase and **b)** Rutile octahedral sites with the 6-fold O atoms.

At high oxygen partial pressures, the principal defects appear to be quadruple ionized Ti-interstitials ($Ti_i^{4\cdot}$), substitutional ions, and Ti^{4+}-ion vacancies ($V_{Ti}^{4'}$). It is well known that some metal species can diffuse inside semiconductors matrix and enter substitutionally in the Ti^{4+}-ion vacancies. There is Electron-Paramagnetic-Resonance evidence that this is the case of the Nb, which enters substitutionally in the TiO_2 matrix as Nb^{5+} ($Nb^{\cdot}_{Ti}$) [29] and, then, the neutrality equation for high oxygen partial pressure becomes,

$$4\left[Ti_i^{4\cdot}\right] + p + \left[Nb^{\cdot}_{Ti}\right] = n + \left[M'_{Ti}\right] + 4\left[V_{Ti}^{4'}\right] \qquad (3.3)$$

where we suppose complete ionization (at working temperature > 500°C), hence Ti-vacancies may compensate Nb-interstitials, even reaching $\left[Nb^{\cdot}_{Ti}\right] = 4\left[V_{Ti}^{4'}\right]$, to give,

$$n = \left(\left[Nb_{Ti}^{\cdot} \right] / K_2 \right)^{1/4} K_i p_{O_2}^{-1/4} \tag{3.4}$$

hence N parameter (equation 1.2, *Chapter 1*) changes from -6 for undoped samples to -4 for Nb-doped ones [30].

Moreover, the incorporation of Nb metal ions in TiO_2 lattice as a substitutional doping does not affect the basic TiO_2 structure (anatase or rutile) [31] as the ionic radii of Nb^{5+} (0.70 Å) is comparable to that of Ti^{4+} (0.68 Å) [6, 9, 32, 33].

3.5.3 Inhibition of the Anatase to Rutile Phase Transition

All our results, the spectroscopic (Raman and XRD) as well as SAED, show an important inhibition of the TiO_2 anatase to rutile phase transition when introducing Nb to our samples. These results have been also clearly corroborated by means of HRTEM, finding that the number of anatase nanoparticles was much higher for those samples with presence of Nb. In order to understand the influence of Niobium in the phase transition mechanism several aspects have to be taken into account. In the following, an explanation of the phase transition inhibition phenomena is proposed.

If we consider defect formation by foreign ions in titania lattice, we can suggest that ions which enter the system substituting Ti^{4+} may either enhance or retard the transformation from anatase to rutile depending on whether the number of oxygen vacancies is increased or decreased [34]. We know that Nb^{5+} ions enter substitutionally occupying Ti^{4+} vacancies. This entrance is possible due to the ionic radii similarity, but in order to assure the material charge neutrality, these Nb^{5+} ions should be compensated by a decreasing of the Oxygen vacancies. As we have seen, if we consider that for the phase transition, a minimum ratio of oxygen vacancies in anatase {112} planes is needed in order to assure the process, then, the extra valence on niobium ions would be the responsible of hindering the transformation to rutile [32, 34].

3.5.4 Grain Growth Inhibition

An important inhibition of the grain growth has been also observed at high annealing temperatures (900 °C) when introducing Nb to our samples. Our TEM results and particle size histogram performed clearly showed an inflexion point for which there is a maximum of inhibition. This point has been found at around 3-4 Nb at. %, where the TiO_2 nanoparticles mean size was around 32 nm. This value has highly increased for the unloaded (up to 130 nm) and also for the high loaded samples (up to 57 nm). By now, we will just discuss the general aspect of the grain growth hindering when loading our samples with Nb. In this way, the results obtained by other authors are also in good agreement with ours [9, 35]. In order to explain the effect observed, we have to take into account that in the incorporation of Nb in titania lattice, the Niobium ions occupy substitutionally titanium sites due to the similarity of their ionic radii. Nevertheless, Nb^{5+} radius (0.70 Å) is a bit bigger than Ti^{4+} radius (0.68 Å). The result of this is that Nb induces stress in titania lattice, which may hinder the growth of anatase and rutile phase crystallites in the material, as found by Sharma et al. [9]. Moreover, we also want to point out that TiO_2 anatase particles have been found to be smaller than rutile ones in a same sample. These phenomena as well as the existence of an inflexion point in grain growth are discussed in the next *Section* when the effects of Nb segregation have been introduced.

3.5.5 NbO Segregation related to Phase Transition

As it has been demonstrated by our HRTEM analysis, there is Niobium segregation out from TiO_2 structure. This segregation has two possible origins depending on its nature: segregation during phase transition and/or segregation at high loading values. In the following, we will discuss when the cases exposed occur.

3.5.4.1 Segregation during Phase Transition

The former explanations suggest that an anatase grain containing Niobium dopants would experience a great difficulty when trying to transform to rutile. In this way, it is plausible to suggest that transformation should be accompanied of a previous Nb segregation, in order to allow an increasing of the oxygen vacancies in our material and let an easier phase transition. The process described could explain the behavior of our anatase nanoparticles when increasing the temperature. In this way, Nb^{5+} ions would remain inside anatase bulk until the temperature is high enough to give the necessary mobility to our Niobium ions to sinter. Thus the Nb aggregates created would be expulsed out from anatase structure and would be finally placed on TiO_2 surface in an oxidized Nb phase. At the same time, once the main part of the Niobium has left the anatase structure, a fast transformation to rutile would happen, since at those high temperatures, the phase transition would be highly favored.

If we consider the Nb segregation on TiO_2 surface, it would be expected that Nb would react with the TiO_2 surface acquiring one of its oxidized phases, thermodynamically more stables than the metallic ones. Recently, Marien et al. [36] calculated, in a simple model, the change of the Gibbs free energy DG^o of the surface reaction, assuming that TiO_2 (rutile) was reduced to Ti_2O_3.

$$2TiO_2 + Nb \rightarrow Ti_2O_3 + NbO \qquad (DG^o = -36 \text{ kJ/mol}), \qquad (3.5)$$

$$4TiO_2 + Nb \rightarrow 2Ti_2O_3 + NbO_2 \qquad (DG^o = -57 \text{ kJ/mol}), \qquad (3.6)$$

$$10TiO_2 + 2Nb \rightarrow 5Ti_2O_3 + Nb_2O_5 \qquad (DG^o = -59 \text{ kJ/mol}). \qquad (3.7)$$

In their work, and after analyzing their specimens, Marien et al. couldn’t determine whether NbO, NbO_2 or Nb_2O_5 was formed. As we can see the thermodynamically most favorable reaction would transform Nb into Nb_2O_5, due to its lower Gibbs free energy value. Controversially, our results found by SAED and HRTEM suggests the presence of NbO clusters on TiO_2 grain surfaces.

After analyzing few hundreds of TiO_2 nanoparticles, we could never find any anatase nanoparticle with NbO clusters on its surface, however, the Niobium EDS signal seemed to come from anatase bulk, meaning that anatase structure let the incorporation of Nb atoms inside it. On the other hand, the presence of NbO clusters on rutile grains surface would confirm our hypothesis in which we have suggested a previous segregation of Nb ions before or during phase transition.

To our knowledge, this is the first time that segregation of Nb is related with the anatase to rutile phase transition.

3.5.4.2 Segregation at High Nb Loading Values

Until now, we have shown the needing of Nb ions segregation out of the anatase structure in order to favor the anatase to rutile phase transition. We pointed out that this segregation is possible when we reach a determinate annealing temperature. Nevertheless, there is another effect that it hasn't been explained yet, and this is the acceleration of phase transformation for high loading values with respect to low loading values. It would be expected a decreasing of the phase transition rate when increasing the Nb loading, but, as observed in our experimental results, there is an inflexion point at around 3-4 Nb at. %, from which the transformation rate would slowly increase again when increasing the Niobium loading up to higher values.

Taking into account the stress induced to the anatase grains by the diffusion of Nb ions inside its structure, we suggest that there is a point in which the excess of stress is not thermodynamically supported anymore, and the structure should reduce it by removing part of the Nb ions. At this point we would reach the solubility limit of the Nb in the TiO_2 anatase structure, and the excess of Nb ions would be segregated out of the grain. In this case Niobium segregation would occur even before than in the grains from low loaded samples, explaining the faster transformation to rutile of high loaded samples.

Moreover, in the case of the highest loaded sample (24.9 % Nb at.), NbO seems to create a thin film composed of few monolayers on TiO_2 rutile grain surfaces. After our HRTEM observations, we suggest that NbO may follow a Volmer-Weber growing mode on TiO_2 surface [37, 38], forming three-dimensional clusters until the quantity of material is high enough to let the clusters merge into a thin film.

3.5.6 Phase Transition and Growth Mechanisms

After all the discussion performed above we are ready to suggest a model of the phase transition and the growing mechanisms.

First of all, we want to point out that there is an intimate relation between grain growth and anatase to rutile phase transition. Both mechanisms are hindered due to the presence of Niobium ions inside anatase bulk, so it is obvious that both will be favored after Nb segregation. In this way, and as previously shown in our experimental results, the undoped sample is the one whose TiO_2 nanoparticles are the fastest changing the structural phase and growing. These ones would be followed by the high loaded samples for which a relative fast segregation of part of the Nb would favor also a fast transition and growth. And finally the TiO_2 grains from low loaded samples, which would keep the Nb ions in the anatase structure until they reach a high annealing temperature. As observed experimentally, there are evidences that the particle phase transition goes from inside to outside of the grain while the segregation of the Nb is produced. Further studies will me made in the nearly future in order to reconfirm and refine the model proposed.

3.6 Conclusions

The present *Chapter* has been devoted to the analysis of the Niobium diffusion influence on TiO_2 semiconductor gas sensor materials. Two main effects have been analyzed: the anatase to rutile phase transition and grain growth inhibition due to the presence of Nb^{5+} ions in the anatase structure.

The results obtained seem to be consistent with the evidence that Nb^{5+} enters substitutionally in the anatase TiO_2 structure. The anatase to rutile phase transition hindering has been observed and analyzed by Raman, XRD and SAED, observing that the lowest transformation rate is given by low loaded samples (around 3 % Nb at.), followed by the high loaded (up to 25 % Nb at.). The phase inhibition has been attributed to the extra valence on niobium ions, which reduces oxygen vacancies in the anatase phase, thus retarding the transformation to rutile.

Moreover, the grain growth rate has been studied by TEM. The grain growth is inhibited due to the stress induced to the anatase structure by the Nb^{5+} substitutional ions, with a slightly higher ionic radius value with respect to Ti^{4+}.

The application of HRTEM and DIP to our analyses has given an innovative point of view to the previous works performed in this matter. Our HRTEM analysis show that niobium is segregated out of the anatase structure just before or even during the phase transformation. The Nb segregation is intimately related with the phase transition and it can be caused by the increasing of the annealing temperature and accelerated in the case of high Nb loading values in order to reduce the structure stress. Once the TiO_2 nanoparticle has segregated the Nb in excess, starts to grow when increasing the temperature. To our knowledge, this is the first time that Nb segregation has been related with phase transition and growth mechanisms.

Nb segregated out of TiO_2 nanoparticles has been always found in its NbO oxidized phase, forming nanoclusters on grain surface and following a Volmer-Weber growing mode until clusters merge into a thin film for high loading values.

To sum up, the general phase transition and growth mechanism proposed would be the following:

1) The presence of Nb substitutional ions in the anatase structure hinders or inhibits the phase transition and growth of the nanopowders.
2) When increasing the annealing temperature, the Nb ions are segregated out of the grains forming oxidized species (we have found NbO forming clusters on grains surface). This segregation would be enhanced when increasing the metal loading percentage due to the higher stress introduced in the anatase structure.
3) Once part of this Nb is out of the anatase structure, the number of Oxygen vacancies would be recovered to assure the crystal charge neutrality, favoring the anatase to rutile phase transition. At the same time, the reduction of the stress induced by Nb ions would favor the grain growth, leading to the formation of bigger TiO_2 rutile nanoparticles, as observed by HRTEM.

The work performed in this *Chapter* can be used in order to improve the knowledge about grain growth and phase transition mechanisms, influenced by the Nb introduction. As we have shown, a good selection of the Nb loading in TiO_2 samples can control the TiO_2 grains growth leading to a higher specific surface nanopowders, which highly enhance the gas sensing properties of the sensor device. Moreover, Nb in low loading values gives to anatase particles a good stability in front of temperature changes, increasing the mean temperature point for phase transition. Furthermore, the introduction of Nb gives more sensitivity to the implemented sensor devices thanks to its important role as catalyst in TiO_2 matrix. A good understanding of these phenomena can help us to improve and tailor the future SGS materials characteristics.

3.7 Appendix: SAED patterns tables

#Ring	d (Å)	planes	Phase	#Spot	d (Å)	planes	Phase
1	3.52	{101}	TiO_2 A	A	3.25	{110}	TiO_2 R
2	2.43	{103}	TiO_2 A	B	2.49	{101}	TiO_2 R
3	2.38	{004}	TiO_2 A	C	2.19	{111}	TiO_2 R
4	2.33	{112}	TiO_2 A	D	2.05	{210}	TiO_2 R
5	1.89	{200}	TiO_2 A				

Table 3.7. SAED pattern profile indexation corresponding to that shown in *figure 3.14.a*, for sample A600. TiO_2 A and TiO_2 R correspond to *Anatase* and *Rutile* phases respectively.

#Ring	D (Å)	planes	Phase	#Spot	d (Å)	planes	Phase
1	3.52	{101}	TiO_2 A	A	3.25	{110}	TiO_2 R
ii	2.43	{103}	TiO_2 A	B	2.30	{200}	TiO_2 R
2	2.38	{004}	TiO_2 A	i	2.98	{011}	NbO
3	1.89	{200}	TiO_2 A	ii	2.43	{111}	NbO
4	1.70	{105}	TiO_2 A	iii	2.11	{002}	NbO

Table 3.8. SAED pattern profile indexation corresponding to that shown in *figure 3.14.b*, for sample B600. TiO_2 A and TiO_2 R correspond to *Anatase* and *Rutile* phases respectively. Notice that spot selected as *ii* coincides with TiO_2 anatase and NbO planes.

#Ring	d (Å)	planes	Phase	#Spot	d (Å)	planes	Phase
1	4.76	{002}	TiO_2 A	A	3.25	{110}	TiO_2 R
2	3.52	{101}	TiO_2 A	B	2.30	{200}	TiO_2 R
3	2.38	{004}	TiO_2 A	C	2.19	{111}	TiO_2 R
4	1.89	{200}	TiO_2 A	i	2.98	{011}	NbO
5	1.70	{105}	TiO_2 A				

Table 3.9. SAED pattern profile indexation corresponding to that shown in *figure 3.14.c*, for sample C600. TiO_2 A and TiO_2 R correspond to *Anatase* and *Rutile* phases respectively.

#Ring	d (Å)	planes	Phase	#Spot	d (Å)	planes	Phase
1	3.52	{101}	TiO_2 A	A	3.25	{110}	TiO_2 R
2	2.38	{004}	TiO_2 A	B	2.30	{200}	TiO_2 R
3	1.89	{200}	TiO_2 A	C	2.19	{111}	TiO_2 R
4	1.70	{105}	TiO_2 A	D	2.05	{210}	TiO_2 R
i	2.98	{011}	NbO	i i	2.11	{002}	NbO

Table 3.10. SAED pattern profile indexation corresponding to that shown in *figure 3.14.d*, for sample D600. TiO_2 A and TiO_2 R correspond to *Anatase* and *Rutile* phases respectively.

#Ring	d (Å)	planes	Phase	#Spot	d (Å)	planes	Phase
1	3.52	{101}	TiO_2 A	A	3.25	{110}	TiO_2 R
2	2.43	{103}	TiO_2 A	B	2.49	{101}	TiO_2 R
3	2.38	{004}	TiO_2 A	C	2.19	{111}	TiO_2 R
4	1.89	{200}	TiO_2 A	D	2.05	{210}	TiO_2 R
5	1.70	{105}	TiO_2 A	i	4.21	{001}	NbO
				i i	2.98	{011}	NbO

Table 3.11. SAED pattern profile indexation corresponding to that shown in *figure 3.14.e*, for sample E600. TiO_2 A and TiO_2 R correspond to *Anatase* and *Rutile* phases respectively.

#Spot	d (Å)	plane	Phase	#Spot	d (Å)	plane	Phase
1	3.52	{101}	TiO_2 A	A	3.25	{110}	TiO_2 R
B	2.49	{101}	TiO_2 R	C	2.30	{200}	TiO_2 R
D	2.19	{111}	TiO_2 R	E	2.05	{210}	TiO_2 R
2	1.89	{200}	TiO_2 A				

Table 3.12. SAED pattern profile indexation corresponding to that shown in *figure 3.15.a*, for sample A900. TiO_2 A and TiO_2 R correspond to *Anatase* and *Rutile* phases respectively.

#Ring	d (Å)	planes	Phase	#Spot	d (Å)	planes	Phase
1	3.52	{101}	TiO_2 A	A	3.25	{110}	TiO_2 R
2	2.38	{004}	TiO_2 A	B	2.49	{101}	TiO_2 R
3	1.89	{200}	TiO_2 A	C	2.19	{111}	TiO_2 R
4	1.70	{105}	TiO_2 A	D	2.05	{210}	TiO_2 R
i	2.98	{011}	NbO	iii	2.11	{002}	NbO

Table 3.13. SAED pattern profile indexation corresponding to that shown in *figure 3.15.b*, for sample B900. TiO_2 A and TiO_2 R correspond to *Anatase* and *Rutile* phases respectively.

#Ring	d (Å)	plane	Phase	#Spot	d (Å)	plane	Phase
1	3.52	{101}	TiO_2 A	A	3.25	{110}	TiO_2 R
2	2.38	{004}	TiO_2 A	B	2.30	{200}	TiO_2 R
3	1.89	{200}	TiO_2 A	C	2.19	{111}	TiO_2 R
4	1.70	{105}	TiO_2 A	i	2.98	{011}	NbO
				ii	2.11	{002}	NbO

Table 3.14. SAED pattern profile indexation corresponding to that shown in *figure 3.15.c*, for sample C900. TiO_2 A and TiO_2 R correspond to *Anatase* and *Rutile* phases respectively.

#Ring	d (Å)	plane	Phase	#Spot	d (Å)	plane	Phase
A	3.25	{110}	TiO_2 R	1	3.52	{101}	TiO_2 A
B	2.49	{101}	TiO_2 R	2	2.43	{103}	TiO_2 A
C	2.19	{111}	TiO_2 R	3	2.38	{004}	TiO_2 A
D	2.05	{210}	TiO_2 R	4	2.33	{112}	TiO_2 A
E	1.69	{211}	TiO_2 R	5	1.89	{200}	TiO_2 A
i	2.98	{011}	NbO	ii	2.11	{002}	NbO

Table 3.15. SAED pattern profile indexation corresponding to that shown in *figure 3.15.d*, for sample D900. TiO_2 A and TiO_2 R correspond to *Anatase* and *Rutile* phases respectively.

#Ring	d (Å)	plane	Phase	#Spot	d (Å)	plane	Phase
A	3.25	{110}	TiO_2 R	1	2.43	{103}	TiO_2 A
B	2.49	{101}	TiO_2 R	2	2.33	{112}	TiO_2 A
C	2.19	{111}	TiO_2 R	3	1.89	{200}	TiO_2 A
D	2.05	{210}	TiO_2 R	i	2.98	{011}	NbO
E	1.69	{211}	TiO_2 R	ii	2.11	{002}	NbO

Table 3.16. SAED pattern profile indexation corresponding to that shown in *figure 3.15.e*, for sample E900. TiO_2 A and TiO_2 R correspond to *Anatase* and *Rutile* phases respectively.

References

1. D. Mardare and P. Hones, Optical dispersion analysis of TiO_2 thin films based on variable-angle spectroscopic ellipsometry measurements, *Materials Science and Engineering B*, **68,** 42–47 (1999).

2. Y. Gao, In-situ IR and spectroscopic ellipsometric analysis of growth process and structural properties of $Ti_{1-x}Nb_xO_2$ thin films by metal-organic chemical vapor deposition, *Thin Solid Films*, **346**, 73-81 (1999).

3. S. Matsushima, Y. Teraoka, N. Miura and N. Yamazoe, Electronic interaction between metal additives and tin dioxide-based gas sensors, *Japanese Journal of Applied Physics*, **27** 1798 (1988).

4. J. Zhu, C. Ren, G. Chen, C. Yu, J. Wu, H. Mu, A new automotive air/fuel sensor based on TiO_2-doped Nb_2O_5 thin film by ion-beam-enhanced deposition, *Sensors and Actuators B*, **32**, 209-213 (1996).

5. K. Zakrzewska, M. Radecka, M. Rekas, Effect of Nb, Cr, Sn additions on gas sensing properties of TiO_2 thin films, *Thin Solid Films*, **310**, 161-166 (1997).

6. R. K. Sharma, M.C. Bhatnagar, G.L. Sharma, Mechanism in Nb doped titania oxygen gas sensor, *Sensors and Actuators B*, **46**, 194-201 (1998).

7. Z. Jianzhong, R. Congxin, C. Guoliang, M. Haichuan, W. Jiali, Y. Chunying, Fabrication and characterisation of a new automotive air-to-fuel sensors based on Pt- and TiO_2-doped Nb_2O_5 film deposited by IBED, *Sensors and Actuators B*, **46**, 180-185 (1998).

8. L.E. Depero, L. Sangaletti, B. Allieri, E. Bontempi, R. Salari, M. Zocchi, C. Casale, M. Notaro, Niobium-titanium oxide powders obtained by laser-laser induced synthesis: Microstructure and structure evolution from diffraction data, *Journal of Materials Researh*, **13 (6)**, 1644-1649 (1998).

9. R. K. Sharma, M.C. Bhatnagar, Improvement of the oxygen gas sensitivity in doped TiO_2 thick films, *Sensors and Actuators B*, **56**, 215-219 (1999).

10. R. K. Sharma, M. C. Bhatnagar, G.L. Sharma, Effect of Nb metal ion in TiO_2 oxygen gas sensors, *Applied Surface Science*, **92**, 647-650 (1992).

11. M.Z. Atashbar, H.T. Sun, B. Gong, W. Wlodarski, R. Lamb, XPS study of Nb-doped oxygen sensing TiO_2 thin films prepared by sol-gel method, *Thin Solid Films*, **326**, 238-244 (1998).

12. M. Ferroni, O. Richard, N. Bonini, M.C. Carotta, V. Guidi, G. Martinelli, F. Roncani, D. Van Dyck, J. Van Landuyt, Development and structural characterisation of Nb-TiO_2 nanosized thick-films as gas sensors, *Proceedings of the 13th European Conference on Solid-State Transducers*, (1999).

13. G. Sverglieri. E. Comini, G. Faglia, M. Z. Atashbar and W. Wlodarski, Titanium dioxide thin films prepared for alcohol microsensors applications, *Sensors and Actuators B*, **66**, 139-141(2000).

14. M. K. Akhtar, S.E. Pratsinis, Dopants in Vapor-Phase Synthesis of Titania Powders, *Journal of the American Ceramics Society*, **75 (12)**, 3408-3416 (1992).

15. E. Cominia, G. Faglia, G. Sberveglieri, Y. X. Li, W. Wlodarski, M. K. Ghantasala, Sensitivity enhancement towards ethanol and methanol of TiO_2 films doped with Pt and Nb, *Sensors and Actuators B*, **64**, 169–174 (2000).

16. M. Musci, M. Notaro, F. Curcio, M.C. Casale, G. De Michele, Laser synthesis of vanadium-titanium oxide catalysts, *Journal of Materials Research*, **7**, 2846-2852 (1992).

17. G. A. Tompsett, G. A. Bowmaker, R. P. Cooney, J. B. Metson, K. A . Rodgers and J. M. Seakins, The Raman Spectrum of Brookite, TiO_2 (Pbca, Z = 8), *Journal of Raman Spectroscopy*, **26**, 57-62 (1995).

18. *JCPDS*, 21-1272 (1997).

19. *JCPDS*, 21-1276 (1997).

20. G. Cerrato, L. Marchese and C. Morterra, Structural and morphological modifications of sintering microcrystalline TiO_2: an XRD, HRTEM and FTIR study, *Applied Surface Science*, **70/71**, 200-205 (1993).

21. R. J. González, Raman, Infrared, X-ray, and EELS Studies of Nanophase Titania, *Ph. D. Thesis*, Blacksburg, Virginia (USA), (1996).

22. *JCPDS*, 43-1290 (1997).

23. *JCPDS*, 09-0235 (1997).

24. *JCPDS*, 44-1053 (1997).

25. *JCPDS*, 37-1468 (1997).

26. *JCPDS*, 39-1407 (1997).

27. R. D. Shannon and J. A. Pask, Kinetics of the anatase-rutile transformation, *Journal of the American Ceramic Society*, **48**, 391-398 (1965).

28. S. Hishita, I. Mutoh, K. Koumoto and H. Yanagida, Inhibition Mechanism of the Anatase-Rutile Phase Transformation by Rare Earth Oxides, *Ceramics International*, **9 (2)**, 61-67 (1983).

29. P.H. Zimmermann, Temperature dependence of the EPR spectra of Niobium-doped TiO_2, *Physical Review B*, **8**, 3917-3927 (1973).

30. J. F. Baumard, E. Gervais, *Phys. Status Solidi* (a) **39**, 373 (1977).

31. A.Bernasik, M. Redeeka, M. Rekes, M. Sloma, Electrical properties of Cr and Nb doped TiO_2 thin films, *Applied Surface Science*, **65-66**, 240-245 (1993).

32. M. C. Carotta, M. Ferroni, D. Gnani, V. Guidi, M. Merli, G. Martinelli, M.C. Casale and M. Notaro, Nonostructured pure and Nb-doped TiO_2 as thick film gas sensors for environmental monitoring, *Sensors and Actuators B*, **58,** 310-317 (1999).

33. M. Ferroni. M. C. Carotta, V. Guidi, G. Martinelli, F. Ronconi, O. Richard, D. Van Dyck and J. Van Landuyt, Structural characterization of Nb-TiO_2 nanosized thick-films for gas sensing application, *Sensors and Actuators B*, **68**, 140-145 (2000).

34. M. K. Akhtar, S. E. Pratsinis and S. V. R. Mastrangelo, Dopants in Vapor-Phase Synthesis of Titania Powders, *Journal of the American Ceramic Society*, **75 (12)**, 3408-3416 (1992).

35. L. E. Depero, L. Sangaletti, B. Allieri, E. Bontempi, A. Marino and M. Zocchi, Correlation between crystallite sizes and microstrains in TiO_2 nanopowders, *Journal of Crystal Growth*, **198/199**, 516-520 (1999).

36. J. Marien, T. Wagner, G. Duscher, A. Koch and M. Rühle, Nb on (110)TiO_2 (rutile):growth, structure, and chemical composition of the interface, *Surface Science*, **446**, 219-228 (2000).

37. U. Diebold, J.-M. Pan and T. E. Madey, Growth mode of ultrathin copper overlayers on TiO_2(110), *Physical Review B*, **47 (7)**, 3868-3876 (1993).

38. B. Joyce, Self-organization yields quantum-dot devices, *Vacuum Solutions*, **17**, 11-14 (2000).